# Ultrasound Imaging-based Closed-Loop Control of Functional Electrical Stimulation for Drop Foot Correction

Qiang Zhang, Member, IEEE, Krysten Lambeth, Ashwin Iyer, Ziyue Sun, and Nitin Sharma\*, Senior Member, IEEE

Abstract—Open-loop or closed-loop functional electrical stimulation (FES) has been widely investigated to treat drop foot syndrome, which is typically caused by weakness or paralysis of ankle dorsiflexors. However, conventional closed-loop FES control mainly uses kinematic feedback, which does not directly capture time-varying changes in muscle activation. In this study, we explored the use of ultrasound (US) echogenicity as an indicator of FES-evoked muscle activation and hypothesized that including US-derived muscle activation, in addition to kinematic feedback, would improve the closed-loop FES control performance compared to the closed-loop control that relies only on the kinematic feedback. A sampled-data observer (SDO) was derived to continuously estimate FES-evoked muscle activations from low-sampled US echogenicity signals. Additionally, a dynamic surface controller (DSC) and a delay compensation (DC) term were incorporated with the SDO, noted as the USbased DSC-DC, to drive the actual ankle dorsiflexion trajectory to a desired profile. The trajectory tracking error convergence of the closed-loop system was proven to be uniformly ultimately bounded based on the Lyapunov-Krasovskii stability analysis. The US-based DSC-DC controller was validated on five participants with no disabilities to control their ankle dorsiflexion during walking on a treadmill. The US-based DSC-DC controller significantly reduced the root mean square error of the ankle joint trajectory tracking by  $46.52\% \pm 7.99\%$ (p<0.001) compared to the traditional DSC-DC controller with only kinematic feedback but no US measurements. The results also verified the disturbance rejection performance of the USbased DSC-DC controller when a plantarflexion disturbance was added. Our control design, for the first time, provides a methodology to integrate US in an FES control framework, which will likely benefit persons with drop foot and those with other mobility disorders.

Index Terms—Functional electrical stimulation, Ankle dorsiflexion, Drop foot, Ultrasound imaging, Sampled-data observer, Nonlinear control

## I. Introduction

Drop foot is a typical symptom of weakened ankle dorsiflexion after stroke [1], [2] and other neurological disorders such as multiple sclerosis [3], incomplete spinal cord lesions

Qiang Zhang, Krysten Lambeth, Ashwin Iyer, Ziyue Sun, and Nitin Sharma are with the UNC & NC State Joint Department of Biomedical Engineering, the University of North Carolina at Chapel Hill and North Carolina State University, Raleigh, NC, USA. (e-mail: {qzhang25, klambet, aiyer3, zsun32, and nsharm23}@ncsu.edu). (\*Corresponding authors: Nitin Sharma)

The paper has supplementary material available on Youtube at https://youtu.be/GZOvznxzkVY.

This work was funded by NSF CAREER Award # 2002261.

[4], etc. Affected persons are unable to exhibit normal foot ground clearance during the swing phase, resulting in unnatural steppage gait to avoid tripping/falls [5]. To correct drop foot, functional electrical stimulation (FES), which is an artificial technique to apply electrical potentials across skeletal muscles, can be placed over the peroneal nerve and the tibialis anterior (TA) muscle to induce orthotic effects at the ankle joint. Since the earlier demonstrations of FES to correct drop foot by Kantrowitz [6] and Liberson [7], recent studies [8]–[10] have concurred with its effective orthotic effects on a larger clinical population.

Traditionally, the TA muscle is activated during the swing phase using discrete sensors that detect either heel contact or leg inclination [9]. Here, FES is applied through an open-loop or a trigger-based control method. The stimulation amplitude is fixed or uses a pre-determined trapezoidal shape [7]. Thus, given the nonlinear and time-varying nature of the FES-activated neuromuscular system, current commercial drop foot stimulators' inability to automatically modulate the stimulation intensity is a major drawback. Furthermore, with the open-loop FES control mode, the users may be tempted to choose a higher intensity than necessary to reach enough dorsiflexion for the ground clearance, which would likely aggravate FES-induced muscle fatigue, and thus reduce the effectiveness of open-loop FES control [11], [12].

Time-varying physiological changes in affected muscles and the requirement to track a desired limb angle trajectory necessitate closed-loop FES control. Feedback can provide robust performance and recreate precise and accurate functional joint movements. The major challenges that implement closed-loop FES include highly nonlinear, time-varying properties of electrically stimulated muscle, electromechanical delay (EMD), muscle fatigue, spasticity, and day-to-day variations. To address these challenges, a range of advanced control strategies have been developed to achieve a satisfactory trajectory tracking performance for either knee joint or ankle joint. For example, the high-gain robust nonlinear control [13], input delay compensation (DC) [14]–[16], adaptive control [17], [18], and model predictive control [19], [20] designs for the FES-elicited knee extension tracking or cycling tasks have been thoroughly investigated. For FES-elicited ankle joint motion control, especially for drop foot correction, the adaptive control [21], [22], iterative learning control [11], [12] and repetitive control [23] designs have been proposed in recently years. However, as yet, FES control designs mostly use joint kinematic data as feedback to address the regulation or tracking problem. Apart from the kinematic data, other solutions have also been applied to the closed-loop FES control on different joints, which could be explored for drop foot correction. These solutions include the force prediction modeling of the elbow joint with the consideration of co-activation [24], the pedal force prediction modeling of FES-elicited cycling [25], and the ankle joint torque estimation based on the FES-evoked EMG [26].

Motivation exists to use measurements of FES-evoked muscle activation and thus enable FES control based on more accurate (third-order) musculoskeletal dynamics. Alibeii et al. [15] developed a proportional-integral-derivative (PID) type controller that used a dynamic surface control (DSC) error structure along with a DC term to account for the muscle activation dynamics and EMD. The FES-evoked muscle activation was estimated based on an identified first-order activation dynamic model, which was parameterized by using off-line system identification [27]. Reasonably, real-time physiological muscle state measurements, if available, would be more favorable than an offline identified muscle activation estimator to capture the time-varying muscle's physiological changes. Surface electromyography (sEMG) is indeed one traditional tool that is employed to measure FES-induced or volitional muscle activation levels. However, sEMG is extremely sensitive to electrical interference [28] because sEMG records electrical activity during muscle contraction via electrodes placed on the skin, which are by necessity near the electrodes used in FES. During the stimulation, FES impulses can severely corrupt the sEMG signals with artifacts [29]. For example, FES can deliver impulses on the order of 100 V while sEMG attempts to record muscle electrical signals that are on the order of <100 mV with an inherently low signal-to-noise ratio (SNR). Therefore, the advanced electrical filter circuits or filtering algorithms are necessary to incorporate sEMG into FES control [30]-[36]. Recently, ultrasound (US) imaging has been proposed as an alternative non-invasive technology to directly visualize skeletal muscle contractility and assess muscle activation levels under both voluntary and FES-elicited joint movement [37]–[41]. Compared to sEMG, US imaging is unaffected by stimulation artifacts during FES. Further, due to its ability to directly visualize the muscle, the derived signals are devoid of interference from the adjacent muscles. However, US imaging is yet to be shown as a feasible real-time sensing modality that can be integrated into closed-loop FES control.

In this paper, for the first time, we show the feasibility of deploying US imaging to detect FES-elicited muscle activation levels and incorporate the US imaging-derived signal in an FES control design. The US imaging-based control framework is validated to track an ankle dorsiflexion trajectory during a treadmill walking task. The main challenge to incorporate US imaging-derived signals in the closed-loop FES control is the low sampling rate of the US imaging-derived feedback signal. The low sampling rate mainly stems from computationally intensive US image generation and its processing. So far, previous US imaging studies processed

and derived volitional [38], [39], [41] or FES-evoked [40], [42] muscle activation data in an offline manner. Thus, to the best of our knowledge, the real-time use of US imaging data to monitor FES-evoked muscle activation and aid its control performance remains unexplored. Specifically, we use the US imaging-derived echogenicity signal for measuring muscle activation, although at a much lower sampling frequency compared to kinematic measurements from inertial measurement units (IMU) or angular encoders, and integrate it with a continuous FES closed-loop control approach. Unlike architectural features that are extracted from US imaging, like pennation angle, fascicle length, muscle thickness, and tissue displacement, US echogenicity refers to the ability to reflect US waves in the context of surrounding tissues [43], which can be visualized as the brightness and darkness of the region of interest (ROI) and calculated as the average brightness of the ROI in each image frame. US echogenicity calculation does not rely on complex and time-consuming dynamic pixel displacement tracking algorithms, which brings potential computational benefits to save processing time in the realtime application. Previous offline studies have demonstrated a good correlation between echogenicity and muscle contractility/activation [41], [42], [44], [45].

To address the challenge of assimilating the lower-sampled US imaging-derived signals, a sampled-measurement databased observer (SDO) is derived to estimate muscle activation levels in a continuous manner. Due to gait-to-gait and personto-person variations, a pre-defined time-dependent desired trajectory needs to be compressed or stretched online to adapt to the walking conditions, which can easily cause a mismatch between gait phases and affect control performance. Therefore, in this study, inspired by virtual constraints in [46], we propose to generate a time-independent desired ankle joint trajectory in joint space based on the portraits of thigh and shank segments from normal gait data obtained from walking on a treadmill. Compared to the preliminary simulation study in [47], in this work, we conducted walking experiments with the US-based DSC-DC control method on a treadmill. The main innovations and contributions of this paper include: 1) derivation of an US-based DSC-DC control framework to handle low-sampled US signals and EMD in FES, 2) trajectory tracking error convergence analysis of the combined observer and controller based on a Lyapunov-Krasovskii functional, 3) time-independent ankle joint desired trajectory generation based on virtual constraints given the portraits of thigh and shank segments, 4) experiments comparing the USbased DSC-DC control method and traditional DSC-DC control method, as well as ankle trajectories comparison between FES-on and FES-off conditions during the swing phase, and 5) evaluation of the disturbance rejection performance during the swing by adding plantarflexion disturbance.

## II. ANKLE JOINT MUSCULOSKELETAL MODEL

# A. Ankle joint dorsiflexion motion dynamics

The dynamic model of the FES-actuated limb movement, as shown in Fig. 1, is given as

$$J\ddot{\theta}(t) + M_v + M_e + M_q + D_{ext} = \tau(t), \tag{1}$$

where  $J \in \mathbb{R}^+$  is the unknown inertia term of the foot along the dorsiflexion axis of rotation, and  $\theta(t)$ ,  $\theta(t)$ , and  $\theta(t) \in \mathbb{R}$ denote the angular position, angular velocity, and angular acceleration, respectively. The constant limb equilibrium point is represented as  $\theta_{eq} \in \mathbb{R}^-$ , which represents the joint's posture when the limb is completely relaxed. The passive moment  $M_v(\theta) \in \mathbb{R}$  is a term to represent musculoskeletal viscosity,  $M_e(\theta) \in \mathbb{R}$  is a term to represent musculoskeletal elasticity, and  $M_g(\theta) = mgl\sin(\frac{\pi}{2} + \theta + \theta_{eq}) \in \mathbb{R}$  is the gravitational term acting on the ankle. The mass of the limb and the length from the limb's center of mass to its rotation center in the sagittal plane are denoted as  $m \in \mathbb{R}^+$  and  $l \in \mathbb{R}^+$ , respectively. The explicit definitions of the functions  $M_v(\dot{\theta})$  and  $M_e(\theta)$  can be obtained from [13], [17]. The term related to external disturbance and unmodeled effects in the neuromusculoskeletal system is denoted as  $D_{ext}(t) \in \mathbb{R}$ .

The limb torque elicited by FES is given as

$$\tau(t) \triangleq r(\theta) F_m \eta_1(\theta) \eta_2(\dot{\theta}) \cos(\alpha) a, \tag{2}$$

where each term on the right hand side is defined in the following properties:

Property 1: The variable  $r(\theta) \in \mathbb{R}^+$  represents the moment arm for the muscle tendon force, which is a function of the joint position, and is given as  $r(\theta) = -0.013(\theta_{eq} - \theta) + 0.035$  [48]. So the moment arm is a continuously differentiable, positive, and bounded function with a bounded first-order time derivative.

Property 2: The variable  $F_m \in \mathbb{R}^+$  represents the constant maximum isometric muscle contraction force at the equilibrium position.

Property 3: Variables  $\eta_1(\theta)$  and  $\eta_2(\dot{\theta})$  denote the nonlinear relationships of force-fascicle length and force-fascicle velocity [49], and both of them are continuously differentiable, non-zero, positive, and bounded functions.

Property 4: The pennation angle between the muscle fascicle and deep aponeurosis, denoted by  $\alpha(\theta) \in \mathbb{R}^+$ , increases monotonically within the approximate range 0-30° as the muscle contracts [50].

Property 5: The variable  $a(t) \in [0, 1]$  denotes the muscle activation level whose ideal dynamics is represented by the following continuous first-order differential equation [51]:

$$\dot{a}(t) = \frac{-a(t) + u(t - \tau_M)}{T_a}. (3)$$

In (3), the EMD caused by FES is denoted as  $\tau_M \in \mathbb{R}^+$  and assumed to be known, and  $T_a \in \mathbb{R}^+$  is the muscle activation decay constant. The normalized non-delayed FES input  $u(t) \in [0,1]$  is due to the boundedness of the muscle stimulation. From [51], the input u(t) is modeled by a piecewise linear function

$$u(t) = \begin{cases} 0, & \bar{u} < u_{\min}, \\ \frac{\bar{u}(t) - u_{\min}}{u_{\max} - u_{\min}}, & u_{\min} \leq \bar{u} \leq u_{\max}, \\ 1, & \bar{u} > u_{\max} \end{cases}$$
(4)

where  $u_{\min}$  and  $u_{\max} \in \mathbb{R}_{\geq 0}$  are the stimulation threshold and stimulation saturation, respectively, and  $\bar{u}(t) \in \mathbb{R}_{\geq 0}$  is the modulated parameter (current, pulse width, or frequency) applied on the TA muscle.

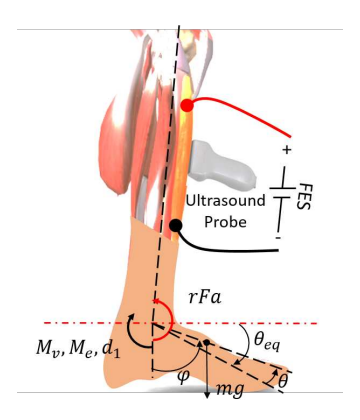


Figure 1: The neuromusculoskeletal schematic of the FES-induced ankle dorsiflexion dynamic system. Notice that only the tibialis anterior muscle is being stimulated, meaning that FES can only produce ankle dorsiflexion and gravity is relied upon to move the foot back to the equilibrium point  $\theta_{eq}$ .

To facilitate the controller development and stability analysis, the following assumptions are made throughout the paper:

Assumption 1: The angular position and velocity signals  $\theta$ ,  $\dot{\theta}$  are continuously measurable.

Assumption 2: The muscle activation signal a is measured by normalizing the US imaging-derived echogenicity signal [41] in a real-time manner, but with a much lower sampling frequency compared to the sampling frequency of the angular position and velocity. The normalized US echogenicity signal is used as muscle activation feedback only at discrete time instant  $t_k$  ( $k=0,1,2,...,\infty$ ), and  $\{t_k\}$  is a monotonically increasing sequence and satisfies  $\lim_{k\to\infty} t_k = \infty$ . The sampling interval is set as a constant value T, namely  $T=t_{k+1}-t_k$ . Due to the data transmission delay, the sampled activation signal is available at instants  $t_k+\tau_k$ , where  $\tau_k>0$  denotes the unknown and timevarying transmission delay with an upper bound  $\bar{\tau}$ . Thus, the maximum time duration between two successively available muscle activation measurements is  $T+\bar{\tau}$ , denoted as  $\bar{T}$ .

Assumption 3: The desired ankle trajectory  $\theta_d \in \mathbb{R}$  and its time derivatives,  $\dot{\theta}_d \in \mathbb{R}$  and  $\ddot{\theta}_d \in \mathbb{R}$ , are bounded.

# B. Sampled-data observer design

Define a state variable  $\boldsymbol{x} = \left[\theta(t),\,\dot{\theta}(t),\,a(t)\right]^T$ . The overall continuous neuromusculoskeletal system can be expressed in state-space form as

$$\begin{bmatrix} \dot{x}_1 \\ \dot{x}_2 \\ \dot{x}_3 \end{bmatrix} = \begin{bmatrix} x_2 \\ \frac{1}{J_{\Gamma}} \left( -f_{\Gamma}(x_1, x_2) - D_{ext\Gamma} + x_3 \right) \\ \frac{-x_3 + u(t - \tau_M)}{T} \end{bmatrix}, \quad (5)$$

where  $f_{\Gamma}(x)=\frac{M_v(x_2)+M_e(x_1)+M_g(x_1)}{\Gamma(x)}$ ,  $\Gamma(x)=r(x_1)F_m\eta_1(x_1)\eta_2(x_2)\cos(\alpha)$ ,  $J_{\Gamma}=\frac{J}{\Gamma(x)}$ , and  $D_{ext\Gamma}=\frac{D_{ext}}{\Gamma(x)}$ . Hereafter, the following assumptions are also made throughout the paper:

Assumption 4: Based on the properties in (2), the function  $\Gamma(x)$  is continuously differentiable, positive, and bounded.

Also, the first-order derivatives of  $\Gamma(x)$  and  $\frac{1}{\Gamma(x)}$  exist and are bounded.

Assumption 5: Based on Assumption 4, the term  $J_{\Gamma}$  is bounded, and its first-order time derivative exists and is bounded. In addition,  $J_{\Gamma}$  satisfies the inequality  $a_1 \|\theta\|^2 \le \Theta^T J_{\Gamma}\Theta \le a_2 \|\theta\|^2$ ,  $\forall \Theta \in \mathbb{R}^n$ , for some known positive constants  $a_1, a_2 \in \mathbb{R}^+$ .

Assumption 6: The external disturbance in the system  $D_{ext}$  in (1) is bounded. Therefore, based on Assumption 4,  $D_{ext\Gamma}$  is also bounded.

According to (5), the state element  $x_3$  is independent from  $x_1$  and  $x_2$ , so the overall system could be considered as a cascade system, and the SDO will be designed for the subsystem related to  $x_3$ . Based on the sampled and delayed muscle activation from US imaging, the continuous-time observer for muscle activation is given as [52]-[54]

$$\dot{\hat{x}}_{3}(t) = -\frac{\hat{x}_{3}(t)}{T_{a}} + \frac{u(t-\tau_{M})}{T_{a}} + \gamma \varepsilon_{3}(t_{k}) 
t \in [t_{k} + \tau_{k}, t_{k+1} + \tau_{k+1}), k = 0, 1, 2, ..., \infty$$
(6)

where  $\gamma \in \mathbb{R}^+$  is the observation gain used for updating the observer which will be subsequently constrained in stability analysis section. The variable  $\varepsilon_3(t_k) = \hat{x}_3(t_k) - x_3(t_k)$  represents a constant value (a zero-order hold) during the time interval  $t \in [t_k + \tau_k, t_{k+1} + \tau_{k+1})$ , is updated at the time point when the US echogenicity is available, and is assumed to be upper bounded by  $\bar{\varepsilon}_3^k \in \mathbb{R}^+$ . Therefore, the observer model is of a hybrid nature with continuous and discrete variables. The continuous observation error is defined as  $\varepsilon_3(t) = \hat{x}_3(t) - x_3(t)$ , and by taking its time derivative and substituting (5) and (6), the observation error dynamics is given as

$$\dot{\varepsilon}_{3}(t) = -\frac{\varepsilon_{3}(t)}{T_{a}} + \gamma \varepsilon_{3}(t_{k})$$

$$t \in [t_{k} + \tau_{k}, t_{k+1} + \tau_{k+1}), k = 0, 1, 2, ..., \infty$$
(7)

## III. CONTROL DEVELOPMENT

# A. Desired joint trajectory planning - high-level control

During human locomotion, overground or on the treadmill, a time-dependent pre-defined desired ankle dorsiflexion trajectory needs to be compressed or stretched to adapt to gait-to-gait and person-to-person variations, which is a cumbersome design process. Therefore, we use a time-independent trajectory generation profile based on virtual constraints [46]. The desired ankle dorsiflexion trajectory was generated online given the orientations and angular velocities of the thigh and shank segments during the locomotion. Consider the term  $h_d(v(q)) \in \mathbb{R}$  ( $q = [\theta_{shank}, \dot{\theta}_{shank}, \theta_{thigh}, \dot{\theta}_{thigh}]^T$ ), a desired virtual constraint function that is represented with the Bezier polynomial as

$$h_d(v(\mathbf{q})) = \sum_{\bar{k}=0}^{M} \varrho_{\bar{k}} \frac{M!}{\bar{k}!(M-\bar{k})!} v^{\bar{k}} (1-v)^{M-\bar{k}}, \quad (8)$$

where  $M \in \mathbb{R}^+$  is an integer equal to the number of Bezier polynomial terms,  $\varrho_{\bar{k}} \in \mathbb{R}$  represents the parameters that are

determined through the optimization mentioned in [55], [56], and  $v \in \mathbb{R}_{\geq 0}$  is calculated as

$$v(\mathbf{q}) = \frac{\theta(\mathbf{q}) - \theta^{+}}{\theta^{-} - \theta^{+}}, \tag{9}$$

where  $\theta^+$  and  $\theta^-$  are the maximum and minimum values of the function  $\theta(\mathbf{q})$ , respectively, and  $\theta(\mathbf{q}) = \bar{\zeta}_0 + \bar{\zeta}_1 \theta_{shank} + \bar{\zeta}_2 \dot{\theta}_{shank} + \bar{\zeta}_3 \theta_{thigh} + \bar{\zeta}_4 \dot{\theta}_{thigh}$  represents the applied phase variable.  $\bar{\zeta}_i \in \mathbb{R}$  (i=1,2,3,4) is selected such that  $\theta(\mathbf{q})$  is monotonically increasing or decreasing. Finally, the desired ankle trajectory  $\theta_d$  during the swing phase is set as  $h_d(v(\mathbf{q}))$ .

To obtain the optimal solution of  $\varrho_{\bar{k}}$  in the Bezier polynomial (8), a genetic algorithm-based particle swarm optimization (GAPSO) [57] was used to minimize the cost function:

$$\min_{\varrho_{\bar{k}}} R = \sum_{i=1}^{N} \left( h_d^i(v(\boldsymbol{q})) - h_m^i \right)^2, \tag{10}$$

where N represents the number of data samples used in the optimization, and  $h_d^i$  and  $h_m^i$  represent the Bezier polynomial-computed and measured ankle dorsiflexion motion values at the  $i^{th}$  time instant, respectively. The GAPSO utilizes kinematics data that were collected from participants with no disabilities at the walking speed of 0.6 m/s. We preferred designing desired ankle trajectories based on Bezier polynomials, compared to other splines, due to their useful properties that are amenable [55] for numerical stability during the optimization.

# B. Low-level control

The control objective is to develop a trajectory tracking controller for an FES-evoked limb motion that takes both kinematic and muscle activation feedback during the controlled motion. Here, we use US imaging-derived muscle activation as feedback in the control design. Due to the computationally intensive US signal beamforming and imaging process, the real-time feedback of a US imaging-derived signal may be sampled at a low rate, compared to a higher sampled kinematic signal. Therefore, an SDO that combines muscle activation dynamics and sparse US imaging measurements is proposed to continuously estimate FES-evoked muscle activation. With the feedback from the SDO and joint kinematics, a PID-type DSC controller plus a DC term is proposed to achieve the trajectory tracking task. The diagram of the proposed framework is shown in Fig. 2 (a).

Remark 1. Compared to the traditional integrator backstepping method, the benefit of the DSC method is to approximate the derivative of the control input with the dynamics of a low-pass filter. Consequently, this approach avoids taking another time derivative, which otherwise would result in an acceleration signal-based control law [15].

The details of the low-level control design are given below.

1) Open-loop error development: The trajectory tracking error for the ankle neuromusculoskeletal system is given as

$$e(t) = x_d(t) - x_1(t),$$
 (11)

where  $x_d(t) \in \mathbb{R}$  is the desired differentiable ankle dorsiflexion trajectory, which is generated online based on the

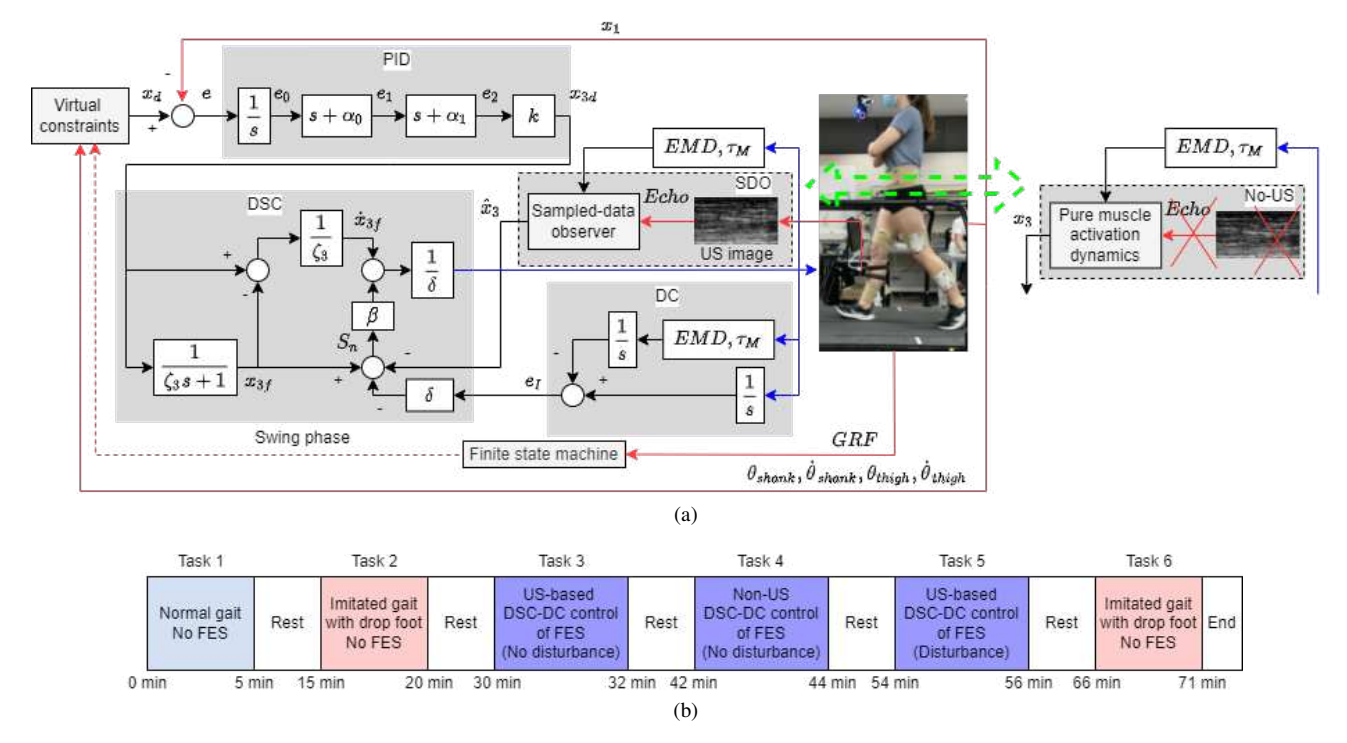


Figure 2: (a) The block diagram of the proposed US-based DSC-DC control framework for the ankle neuromusculoskeletal system during walking on an instrumented treadmill. Virtual constraints were used to generate the desired ankle joint trajectory online during the walking swing phase. The finite state machine was used to differentiate the swing phase and stance phase during walking based on the ground reaction force. Black lines and arrows represent the flows after the intermediate data processing, red solid lines and arrows represent the direct measurements from the treadmill walking experiments, the red dashed line represents the binary state of the swing or stance phase, and blue lines and arrows represent the non-delayed control signals (FES pulse width modulation) to the ankle neuromusculoskeletal system, respectively. The diagram could be shifted to the DSC-DC control framework by changing the "SDO" part to the "No-US" part (shown to the right of the green arrow). (b) The block diagram of the treadmill walking tasks sequence on each participant.

aforementioned virtual constraints. For facilitating control design and stability analysis, the following auxiliary error signal  $e_1(t) \in \mathbb{R}$  is defined as

$$e_1(t) = \dot{e}_0(t) + \alpha_0 e_0(t),$$
 (12)

where  $\alpha_0 \in \mathbb{R}^+$  is a control gain and  $e_0(t)$  is a designed term to incorporate integral control, which is defined as

$$e_0(t) = \int_0^t e(s)ds.$$
 (13)

Another auxiliary error signal  $e_2(t) \in \mathbb{R}$  is defined as

$$e_2(t) = \dot{e}_1(t) + \alpha_1 e_1(t),$$
 (14)

where  $\alpha_1 \in \mathbb{R}^+$  is a control gain. After taking the time derivative of  $e_2(t)$ , multiplying with  $J_{\Gamma}$ , and using (5), (11)-(13), we get the open-loop error dynamics

$$J_{\Gamma}\dot{e}_{2} = J_{\Gamma}\ddot{x}_{d} + f_{\Gamma} + D_{ext\Gamma} - x_{3} + J_{\Gamma}(\alpha_{0} + \alpha_{1})\dot{e} + J_{\Gamma}\alpha_{0}\alpha_{1}e.$$
(15)

2) Backstepping design and dynamic surface control: By introducing a desired virtual control input signal as  $x_{3d} \in \mathbb{R}_{\geq 0}$ , the filtered desired signal, denoted as  $x_{3f}$ , is obtained by passing  $x_{3d}$  through a low-pass filter such that

$$x_{3d} = \zeta_3 \dot{x}_{3f} + x_{3f}, \ x_{3d}(0) = x_{3f}(0),$$
 (16)

where  $\zeta_3 \in \mathbb{R}^+$  is the low-pass filter time constant. By defining the filtering error as  $y_f = x_{3d} - x_{3f}$ , the time derivative of the filtered intermediate signal is a continuously differentiable function and expressed as  $\dot{x}_{3f} = \frac{y_f}{\zeta_3}$ . By defining the surface error as  $S = x_{3f} - \hat{x}_3$ , and adding and subtracting  $x_{3d}$  and  $\hat{x}_3$ , the open-loop error dynamics (15) can also be written as

$$J_{\Gamma}\dot{e}_{2} = J_{\Gamma}\ddot{x}_{d} + \varepsilon_{3} + S + y_{f} - x_{3d} + D_{ext\Gamma} + f_{\Gamma} + J_{\Gamma}(\alpha_{0} + \alpha_{1})\dot{e} + J_{\Gamma}\alpha_{0}\alpha_{1}e.$$

$$(17)$$

By adding and subtracting  $\frac{1}{2}\dot{J}_{\Gamma}e_2$  and a DC term,  $e_I\in\mathbb{R}$ , multiplied by a constant gain  $\delta\in\mathbb{R}^+$ , where  $e_I(t)=\int_{t-\tau_M}^t u(s)ds$ , the rearranged format of (17) can be given as

$$J_{\Gamma}\dot{e}_{2} = -\frac{1}{2}\dot{J}_{\Gamma}e_{2} + S + y_{f} - \delta e_{I} + \varepsilon_{3} + \tilde{\mathcal{H}} + \mathcal{O} - x_{3d} - e_{1}, \tag{18}$$

where the auxiliary signals  $\tilde{\mathcal{H}}(e, e_1, e_2, e_I, x_d, \dot{x}_d, \ddot{x}_d, t) \in \mathbb{R}$  and  $\mathcal{O}(x_d, \dot{x}_d, \ddot{x}_d, \Gamma, t) \in \mathbb{R}$  are defined as

$$\tilde{\mathcal{H}} = \mathcal{H} - \mathcal{H}_d, \ \mathcal{O} = D_{ext\Gamma} + \mathcal{H}_d 
\mathcal{H} = \frac{1}{2}\dot{J}_{\Gamma}e_2 + J_{\Gamma}\ddot{x}_d + f_{\Gamma} + \delta e_I + e_1 
+ J_{\Gamma}(\alpha_0 + \alpha_1)\dot{e} + J_{\Gamma}\alpha_0\alpha_1 e 
\mathcal{H}_d = J_{\Gamma}d\ddot{x}_d + f_{\Gamma}(x_d, \dot{x}_d)$$
(19)

where 
$$J_{\Gamma d} = \frac{J}{\Gamma(x_d)}$$
 and  $f_{\Gamma}(x_d, \dot{x}_d) = \frac{M_v(\dot{x}_d) + M_e(x_d) + M_g(x_d)}{\Gamma(x_d)}$ . Furthermore, according to

Assumptions 1, 2, 4, and 5, the two auxiliary signals  $\tilde{\mathcal{H}}$  and  $\mathcal{O}$  can be bounded as

$$\left| \tilde{\mathcal{H}} \right| \le \rho \left( \|z\| \right) \|z\|, \ |\mathcal{O}| \le \zeta,$$
 (20)

where  $\zeta \in \mathbb{R}^+$  is a known constant,  $\rho(\|z\|) \in \mathbb{R}^+$  is a positive globally invertible non-decreasing bounded function, and z is defined as

$$z = [e_0, e_1, e_2, e_I]^T$$
. (21)

In the expression (18), the desired intermediate signal is defined as [15]

$$x_{3d} = Ke_2 = K\dot{e} + (\alpha_0 + \alpha_1)Ke + K\alpha_0\alpha_1e_0,$$
 (22)

where  $K=K_1+K_2+K_3\in\mathbb{R}^+$ , which implies a PID type signal with three different control gains, and the corresponding coefficients are defined as  $K_p=(\alpha_0+\alpha_1)K,\,K_d=K,$  and  $K_i=K\alpha_0\alpha_1.$ 

By using the definition in (22), (18) can be rewritten as

$$J_{\Gamma}\dot{e}_{2} = -\frac{1}{2}\dot{J}_{\Gamma}e_{2} + S_{n} + y_{f} + \varepsilon_{3} + \tilde{\mathcal{H}} + \mathcal{O} - Ke_{2} - e_{1},$$
 (23)

where  $S_n = S - \delta e_I$ , which is the augmented surface error that contains the DC term  $\delta e_I$ . By substituting the surface error and (6), the time derivative of  $S_n$  is given as

$$\dot{S}_{n} = \frac{y_{f}}{\zeta_{3}} + \frac{\hat{x}_{3}}{T_{a}} - \delta u(t) - \gamma \varepsilon_{3} (t_{k}) + \left(\delta - \frac{1}{T_{a}}\right) u(t - \tau_{M}) ,$$
(24)

The DC term  $e_I$  is proposed to replace the delayed input in the muscle activation dynamics with a non-delayed input. By manipulating the non-delayed input, which is defined as the control law u(t) as

$$u(t) = \frac{1}{\delta} \left[ \beta S_n + \frac{y_f}{\zeta_3} \right], \tag{25}$$

where  $\beta \in \mathbb{R}^+$  is a control gain, we can get the closed-loop surface error dynamics as below

$$\dot{S}_n = -\beta S_n + \frac{\hat{x}_3}{T_a} + \left(\delta - \frac{1}{T_a}\right) u(t - \tau_M) - \gamma \varepsilon_3(t_k).$$
 (26)

## C. Stability Analysis

**Lemma 1.** For any given positive definite matrix  $M \in \mathbb{R}^{n \times n}$ , a positive scalar  $\alpha$ , and a vector function  $\nu$ , the following Cauchy Schwarz inequality always holds as

$$\left[\int_0^\alpha \nu(s)ds\right]^T M \left[\int_0^\alpha \nu(s)ds\right] \leq \alpha \left[\int_0^\alpha \nu^T(s)M\nu(s)ds\right].$$

The proof for this Lemma can be found in [58].

**Theorem 1.** Consider the neuromusculoskeletal system in (5) with a known EMD  $\tau_M$ , by using the TA muscle activation estimation from the SDO with sparse US imaging-derived muscle activation update in (6) and control law in (25), the FES-elicited ankle dorsiflexion trajectory tracking error is ensured to be semi-globally uniformly ultimately bounded (SGUUB) in a sense that

$$|e| < \sigma_0 \exp(-\sigma_1 t) + \sigma_2, \tag{27}$$

where  $\sigma_1$ ,  $\sigma_2$ ,  $\sigma_3 \in \mathbb{R}^+$  are subsequently defined in the stability analysis, provided that the observation gain  $\gamma$  and control gains  $\alpha_0$ ,  $\alpha_1$ ,  $K_1$ ,  $K_2$ ,  $\beta$ ,  $\delta$ , and  $\zeta_3$  satisfy the following sufficient conditions:

$$\alpha_0 \ge \frac{1}{2}, \ \alpha_1 \ge \frac{1}{2}, \ K_1 \ge \frac{3}{2}, \ \frac{1}{\zeta_3} \ge \frac{1}{2} + \frac{\bar{\eta}^2}{2\epsilon}, \ K_2 \ge \frac{\rho^2(\|z\|)}{4\xi},$$
$$0 < \gamma \le (2 - T_a)T_a^{-1} \left(2\bar{T} + 1\right)^{-1},$$
$$\beta \ge \max\left\{\frac{1}{2}\left(-\vartheta + \sqrt{\vartheta^2 + 4\tau_M\delta^{-2}}\right),$$
$$\frac{1}{2}\left(\kappa^{-1}\tau_M\delta^{-2} + \sqrt{\kappa^{-2}\tau_M^2\delta^{-4} + 4\kappa^{-1}\tau_M\delta^{-2}\zeta_3^{-1}}\right)\right\},$$

where  $\epsilon$  is a arbitrary positive constant, and  $\bar{\eta}$ ,  $\xi$ ,  $\vartheta$ , and  $\kappa$  are positive constant values defined in the attached stability analysis, which is detailed in the Appendix.

Proof: Please see the Appendix section.

# IV. EXPERIMENTAL IMPLEMENTATION

As previously stated, it is hypothesized that the consideration of US imaging-derived muscle activation updates would result in a more accurate muscle activation estimation when FES is applied, when compared with the muscle activation that is calculated based on the pure dynamic model in (3). Subsequently, the use of accurate muscle activation in the closed-loop FES control and the DSC+DC would improve the control performance. To validate this hypothesis and demonstrate the efficacy of the newly developed US-based DSC-DC controller, it was tested for an ankle dorsiflexion trajectory tracking task during the walking swing phase to deal with the drop foot problem. Furthermore, it was compared with a traditional DSC-DC controller with the pure offline identified muscle activation dynamics. In addition, given that the ultimate goal of the controller is to improve ground clearance due to drop foot, the ankle joint trajectories during the walking swing phase with controlled FES and without FES were also compared and analyzed.

#### A. Experimental apparatus and protocol

The study was approved by the Institutional Review Board (IRB) at North Carolina State University (IRB number: 20602). Five young participants (identified as A01, A02,..., A05, 3M/2F, age:  $25.4 \pm 3.1$  years, height:  $1.77 \pm 0.10$  m, mass:  $78.0 \pm 21.1$  kg) without any neuromuscular or orthopedic disorders were recruited in this study. Every participant was familiarized with the experimental procedures and signed an informed consent form before participation.

To identify the individual muscle activation decay constant  $T_a$  and EMD  $\tau_M$ , each participant was configured with an isometric condition, as shown in previous studies [39], [41], and a step FES input was applied to the TA muscle. Three steps were conducted to extract parameters of  $T_a$  and  $\tau_M$  from the input FES signal and the dorsiflexion torque measurements. Firstly, the EMD  $\tau_M$  was determined by measuring the time difference from the instant when the FES was applied to the instance when the measured torque began to increase. Secondly, the normalization of

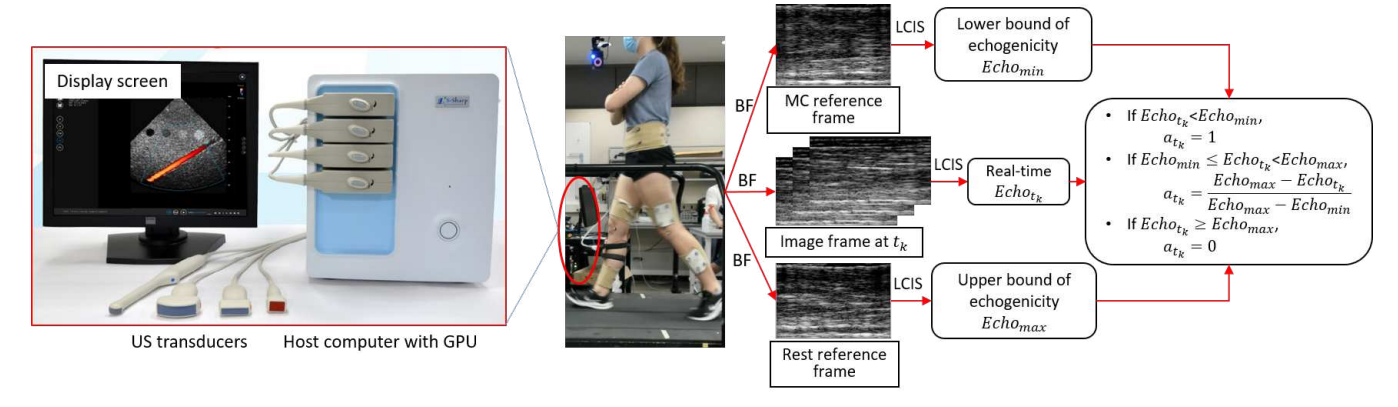


Figure 3: Illustration of the US equipment setup during the treadmill walking experiments and schematic diagram of US echogenicity-derived muscle activation calculation during the walking swing phase. BF-beamforming, MC-maximum muscle contraction at FES saturation, LCIS-logarithmically compressed imaging signal.

Table I: Results of muscle activation decay constant  $T_a$  and EMD  $\tau_M$  from the system identification testing under isometric configuration on individual participants.

Participant	A01	A02	A03	A04	A05	Mean	SD
$T_a$ [s]	0.26	0.41	0.33	0.24	0.30	0.31	0.07
$ au_M$ [ms]	103	121	108	118	95	109	10

the measured dorsiflexion torque was shifted to the left by the EMD value to account for the input delay period. Thirdly, under the assumption that the muscle activation dynamic model is a first-order system, the activation decay constant was identified by solving the time constant that produced the minimal error between the normalized shifted torque measurement and the normalized response of the first-order system with a normalized step input signal. Results of individual  $T_a$  and  $\tau_M$  values from the above identification steps are summarized in Table I.

The main experimental procedures are walking tasks at 0.6 m/s under different conditions on an instrumented treadmill (Bertec Corp., Columbus, OH, USA) with two split belts. Two in-ground force plates (AMTI, Watertown, MA, USA) mounted under two split belts were used to measure ground reaction force (GRF), which was used to differentiate stance phase and swing phase within a gait cycle. The swing phase was triggered when the GRF's z-axis value was less than 5% of each participant's body mass with a unit of kg. Two low-cost 6-axis IMUs (MPU 9250, TDK InvenSense Headquarters, CA, USA) were attached to the right shank and right thigh to measure the 2-D motion in the sagittal plane. The pitch orientations of the shank and thigh segments were determined by using a complementary filtering method, as detailed in [59]. An ankle brace with an incremental encoder (1024 pulses per revolution, TRD-MX1024BD, AutomationDirect, GA, USA) was attached to the right ankle joint to measure the angular position and velocity of dorsiflexion and plantarflexion. A pair of electrodes (size: 2"×2") were placed on the fibular head and the distal belly of the TA muscle, respectively, to pass the biphasic stimulation pulse trains generated by a commercial stimulator (Rehastim 2, HASOMED GmbH, Germany). A

clinical linear US transducer (L7.5SC Prodigy Probe, S-Sharp, Taiwan) with 128 channels was attached to the TA muscle belly perpendicularly by a customized 3D printed holder [39] to image the targeted region in a longitudinal direction. The depth of US imaging was set as 40 mm to include the entire TA muscle area.

We performed six walking tasks on each participant at a speed of 0.6 m/s. The details are given below and also shown in Fig. 2 (b):

Task 1: This task was used for determining the parameters of the Bezier polynomial, via the GAPSO method, to generate the desired ankle joint trajectory online in Tasks (3-5). Here, we asked each participant to walk normally (with preferred ankle dorsiflexion and plantarflexion during the swing and stance phases) on the treadmill for five minutes.

Task 2: Here the task was to imitate the drop foot pattern during the walking swing phase on unimpaired participants. We asked each participant to walk with an imitated drop foot (without voluntary TA muscle contraction during the swing phase) on the treadmill for five minutes. This task might be repeated if there was no significant difference in the ankle joint trajectories during the swing phase in Task 1.

Task 3: In this task we verified the drop foot correction performance by using the proposed US-based DSC-DC control framework. We asked each participant to keep the same walking pattern as in Task 2 while the proposed US-based DSC-DC control framework was applied during the swing phase to assist ankle dorsiflexion by stimulating only the TA muscle and tracking the online generated desired trajectory (the virtual constraint model was optimized by using data collected from Task 1).

Task 4: In Task 4, we compared the drop foot correction performance of Task 3 with that of the DSC-DC control framework without US feedback. Similar experimental procedures as in Task 3 were used, but a traditional DSC-DC controller without US echogenicity-derived muscle activation update was used.

Task 5: This task evaluated the disturbance rejection performance by using the proposed US-based DSC-DC control framework. Similar experimental procedures as in Task 3, but the lateral and medial gastrocnemius muscles were also stimulated with a relatively low constant stimulation intensity during the swing phase.

Task 6: Here we re-evaluated the imitated drop foot pattern during the walking swing phase after removing all FES intervention. The experimental procedures in Task 2 were repeated.

During the experiments, Task 1, Task 2, and Task 6 were always performed in the same order, whereas the order of control Tasks (3-5) was randomly selected. During the experimental procedures from Task 2 to Task 6, the participants were not allowed to view the online generated desired trajectory or the ankle joint performance in real-time. A minimum 10-minute rest period was provided for participants between two successive tasks to avoid muscle fatigue. For Task 1, Task 2, and Task 6, only the measurements data within the middle two minutes were collected for analysis, while for Task 3, Task 4, and Task 5, to avoid FES-induced muscle fatigue, each walking trial lasted two minutes, and data throughout the trial were collected for analysis. A realtime target machine (Speedgoat Inc., Liebefeld, Switzerland) and analog and digital data acquisition boards IO 101 and IO 306 were used to record GRF, IMUs, and encoder signals at 1000 Hz. The controllers in Tasks 3-5 were programmed in Simulink (R2019b, MathWorks Inc., MA, USA) and implemented on the target machine with a frequency of 1000 Hz. The control Tasks required the EMD value and the activation decay constant for the activation state estimators with and without the US imaging-derived update. These values were determined using a system identification experiment conducted on a different day before the treadmill walking experiments under the isometric dorsiflexion condition, which is detailed in [20]. The biphasic stimulation pulse trains had a frequency of 33 Hz, and the current amplitude was set as 20 mA for all participants, while the pulse width was modulated between the subjective threshold and saturation automatically by the controllers. Also, the threshold and saturation of the stimulation pulse width were determined using the same isometric dorsiflexion experiment [20].

# B. US echogenicity-derived muscle activation calculation

Figure 3 presents the illustrative diagram for the US imaging-derived low-sampled muscle activation measurements. Offline studies [41], [42] have shown that US echogenicity has a promising performance regarding volitional and FES-evoked ankle dorsiflexion effort prediction, indicating a good correlation between the US echogenicity and the muscle activation. Therefore, in this study, US echogenicity is used as a measurement of FES-induced muscle activation. The radio frequency data from the US machine were online beamformed based on a line-by-line beamforming method [60]. The echogenicity value from the US image at time instant  $t_k$  is calculated as

$$Echo_{t_k} = \frac{1}{N_A N_L} \sum_{x=1}^{N_A} \sum_{y=1}^{N_L} I_{t_k}(x, y),$$
 (28)

where  $N_A$ ,  $N_L \in \mathbb{R}^+$  represent the pixel numbers along axial and lateral directions, respectively. The term  $I_{t_k}(x, y) \in \mathbb{R}$ represents the US intensity information at the pixel location (x, y) on the image at  $t_k$  instant from the logarithmically compressed imaging signals after the beamforming procedure. Therefore, the 2D map time sequence is transferred to a 1D signal time sequence. Visually, if the individual pixel intensity information is normalized to the gray-scale value (between 0 and 255), it will present the brightness of each pixel on the 2D map. Thus, the calculated echogenicity signal represents the overall brightness within the region of interest. Our previous studies showed that there is a strong negative correlation between the echogenicity change and the muscle contraction level (known as muscle activation here) [41]. Therefore, here, the US echogenicity-derived muscle activation is calculated as the following piecewise function

$$a_{t_k} = \begin{cases} 1, & Echo_{t_k} < Echo_{\min} \\ \frac{Echo_{\max} - Echo_{t_k}}{Echo_{\max} - Echo_{\min}}, & Echo_{\min} \le Echo_{t_k} < Echo_{\max} \\ 0, & Echo_{t_k} \ge Echo_{\max} \end{cases}$$
(29)

where  $Echo_{\rm max}$  and  $Echo_{\rm min}$  are the individual upper and lower bounds of echogenicity signals that are determined under the muscle rest condition and the maximum stimulation condition (with individual FES saturation). The prior testings showed the real-time US echogenicity data was transferred from the US machine to the FES control system at a rate of 7.8 frames per second, which indicates the US imaging-derived muscle activation measurement is sampled at 7.8 Hz.

#### V. RESULTS AND DISCUSSION

# A. Results of online desired trajectory generation

The ankle joint's angular position measurements and the shank's and thigh's orientations and angular velocities during the swing phases of 30 stabilized walking gait cycles were collected in Task 1 across five participants. The data were used to optimize the parameters  $\varrho_k$  in the Bezier polynomial (8), which generated the desired ankle joint trajectory for each participant in control Tasks 3-5. The joint kinematic patterns (shank's and thigh's orientations and angular velocities) during the swing phase across gait cycles facilitated the generation of the desired ankle joint trajectory via GAPSO. In Fig. 4, the time-independent desired trajectories generated based on the virtual constraints and the measured trajectories during 10 exampled gait cycles in Task 1 are depicted for each participant. Given the current study only focused on the swing phase, the desired ankle joint trajectories only exist in the gray areas and are represented by the red curves in Fig. 4 while the measured trajectories are represented by the blue curves. The accuracy of the online trajectory generation based on the virtual constraints was evaluated by calculating the averaged root mean square error (RMSE) values between the virtual constraint-calculated trajectories and measured trajectories during the 30 gait cycles in Task 1 for each participant. These averaged RMSE values are 1.49°, 1.26°, 2.12°, 1.83°, and 1.78° of participant A01, A02,..., A05, respectively. The mean and standard deviation (SD) of

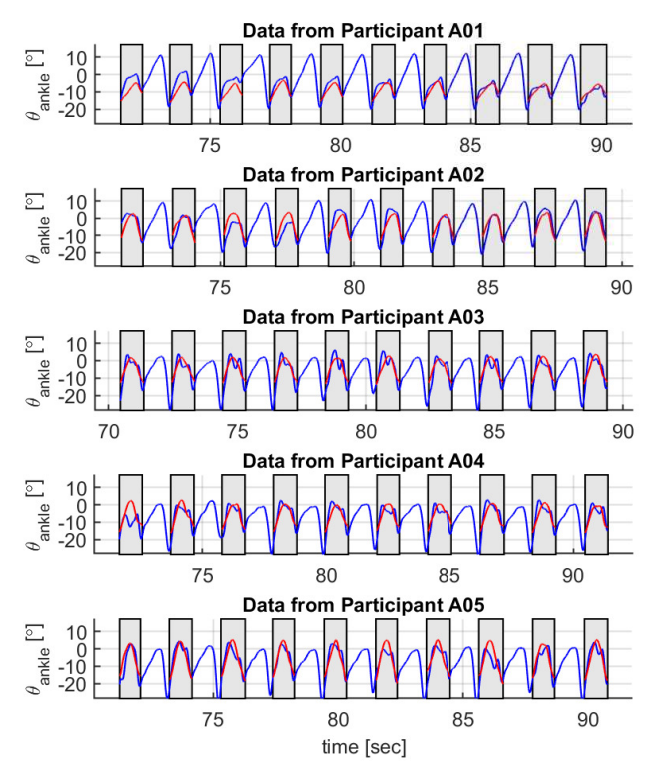


Figure 4: Ankle joint trajectory measurements and results from the GAPSO during the walking swing phase for each participant in *Task* 1. The gray and non-gray areas represent the swing phase and stance phase, respectively. The red and blue curves represent the online generated desired trajectories based on the virtual constraint and the measured trajectories by using the incremental encoder, respectively.

averaged RMSE values across participants are  $1.70\pm0.33^{\circ}$ . The small averaged RMSE value across gait cycles and participants indicates the high robustness of the designed virtual constraints.

# B. Results of control performance

Figure 5 demonstrates the snapshots of one swing phase during Task 3 on Participant A03, where (A) - (H) represent every 12.5% of the swing phase in the current gait cycle. Visually, the ankle joint's angular position is improved in the clockwise direction, especially from (E) to (H), when compared to results from Task 2. In Fig. 6, the quantitative results of ankle joint real trajectories from 30 swing phases in Task 1, Task 2, and Task 3 on each participant are presented, where the black, blue, and red solid curves represent the mean value from 30 selected swing phases, while the black, blue, and red shadowed areas represent the SD in Task 1, Task 2, and Task 3, respectively. It is not surprising that the individual TA muscle had different response and the individual ankle joint had different trajectories due to three main reasons. First, in the current study, we only focused on the treadmill walking swing phase, where the ankle joint was in the air. According to the subjective walking habit, it is reasonable that each participant has a preferred and

comfortable ankle joint trajectory during his or her walking swing phase even though the participant was asked to avoid volitional TA muscle contraction (make the ankle joint at rest) during each walking swing phase. Second, to get the measurements of angular position and velocity on the ankle joint, we attached an ankle-foot brace with an incremental encoder (same for all participants) in the experimental setup. The stabilization of the ankle-foot brace during the walking swing phase depended on many factors, including the size of individual shoes, the tightness of individual shoes, the stiffness and damping parameters of individual ankle joint with the ankle-foot brace, and so on. Third, due to the person-to-person variations, the threshold and saturation of FES pulse width were different between participants, and the control output FES pulse width were time-varying and different between participants. For each swing phase in Fig. 6, the averaged  $\theta_{ankle}$  is calculated, denoted as  $\bar{\theta}_{ankle}$ , then the mean and SD values of 30  $\bar{\theta}_{ankle}$ s on each participant is calculated and shown in Table II. The results show that the right ankle joint real dorsiflexion motion is significantly improved by using the proposed US-based DSC-DC control framework in Task 3 compared to the dorsiflexion motion with imitated drop foot in Task 2. However, compared to the normal gait in Task 1, some inconsistencies still existed even the proposed control framework was applied in Task 3, especially during the first half of the swing phase on Participant A01, A02, and A04.

Table II: Mean and SD values of ankle joint real trajectories in 30 swing phases in *Task* 1, *Task* 2, and *Task* 3 on each participant. (Unit: °)

Condition	Task 1		Task	: 2	Task 3		
Participant	Mean	SD	Mean	SD	Mean	SD	
A01	-4.16	5.96	-19.80	2.19	-11.57	4.69	
A02	-7.76	4.77	-17.36	5.62	-8.32	7.67	
A03	-7.09	2.67	-14.55	5.44	-7.62	4.75	
A04	-3.73	3.74	-23.61	5.67	-5.38	5.21	
A05	-0.74	4.01	-11.12	3.26	-1.66	4.41	
Mean	-4.70	4.23	-17.28	4.43	-6.91	5.35	

By taking Participant A03 as an example, the results of the sparse US echogenicity measurements and the US echogenicity-derived muscle activation levels in tasks 1, 2, and 3 are presented in Fig. 7 (a) and (b), respectively. Among these three tasks, FES was applied only in Task 3, so the input (normalized FES pulse width from the US-based DSC-DC control framework) and output signals (continuous muscle activation estimation given  $T_a=0.33$  s for this participant and  $\gamma=20$ ) of the SDO are presented in Fig. 7 (c) and (d), respectively. In each subplot, the mean and SD of each signal from 30 swing phases are normalized proportionally to the swing phase cycle (0-100%). Results in Fig. 7 (a) and (b) indicate that muscle activation levels in Task 2 are much lower when compared to those in Task 1 and Task 3.

The experimental results for the trajectory tracking performance from a representative participant are presented in Fig. 8, where data were obtained from 10 gait cycles in both *Task* 3 and *Task* 4. The dashed red and solid blue curves respectively represent the desired (generated online based on the virtual constraints) and actual (measured by the

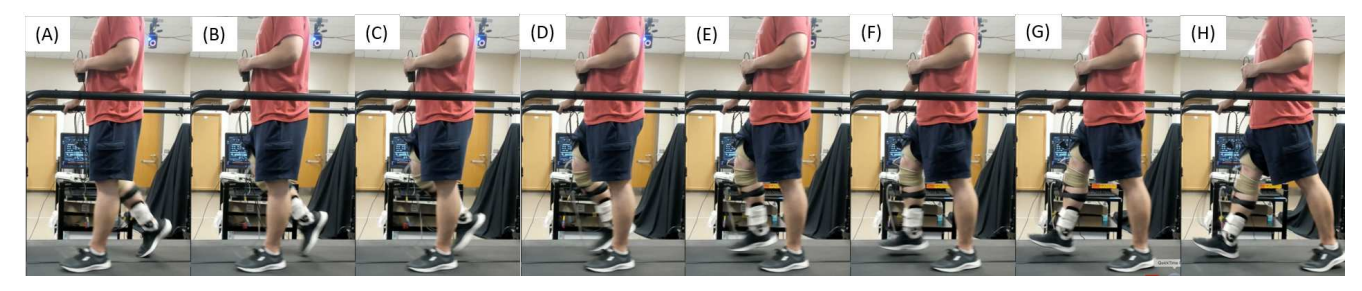


Figure 5: Snapshots of Participant A03's walking swing phase in *Task* 3. (A) to (H) represent every 12.5% of the swing phase in the current gait cycle. The dorsiflexion range of motion is significantly enhanced in *Task* 3 than that in *Task* 2.

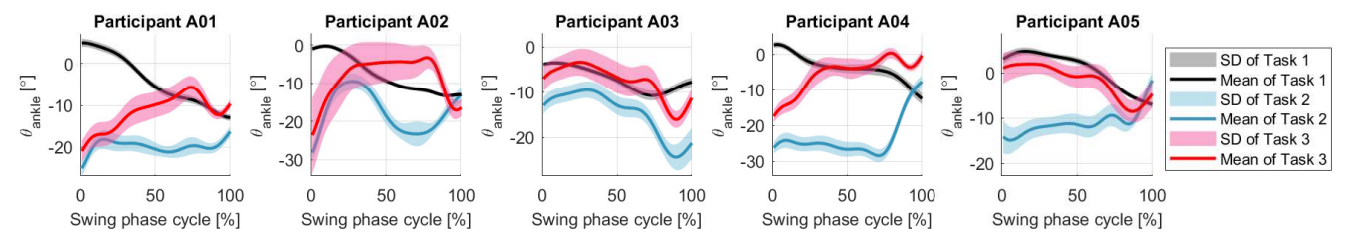


Figure 6: The mean and SD values of ankle joint real trajectories from 30 swing phases of each participant in *Task* 1 (black curves and shadowed areas), *Task* 2 (blue curves and shadowed areas), and *Task* 3 (red curves and shadowed areas).

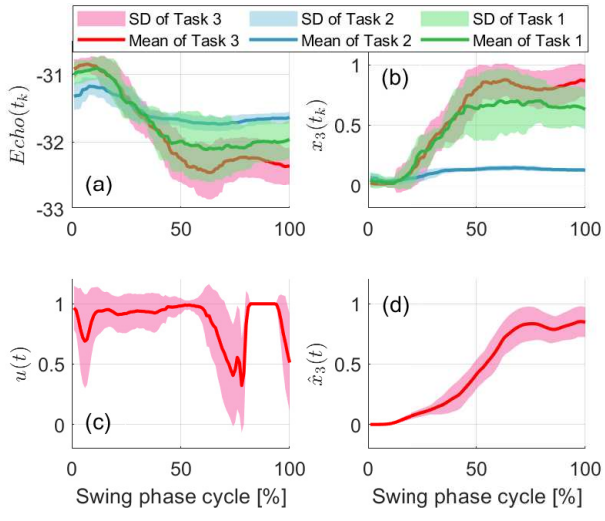


Figure 7: Results of the sparse US echogenicity measurements (a) and the US echogenicity-derived muscle activation levels (b) in *Tasks* 1, 2, and 3, the non-delayed FES normalization from the US-based DSC-DC controller (c) and the continuous estimation of TA muscle activation from the proposed SDO (d) on Participant A03. Each solid curve and shadowed area represent the mean and SD of the corresponding data from 30 swing phases and are normalized proportionally to the swing phase cycle (0 - 100%).

encoder) trajectories. When the US-based DSC-DC controller was applied, the best 10 successive gait cycles from this participant result in the RMSE of  $3.39\pm0.57^{\circ}$ , while when the traditional DSC-DC controller was applied, the best 10 successive gait cycles from this participant result in the RMSE of  $4.55\pm1.42^{\circ}$ . For the RMSE values from the corresponding 10 gait cycles shown in Fig. 8, a two-sample

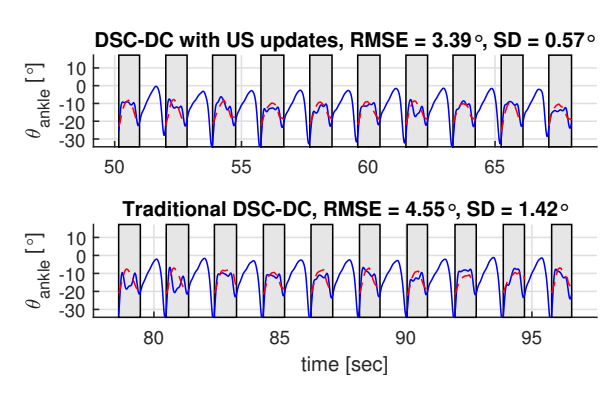
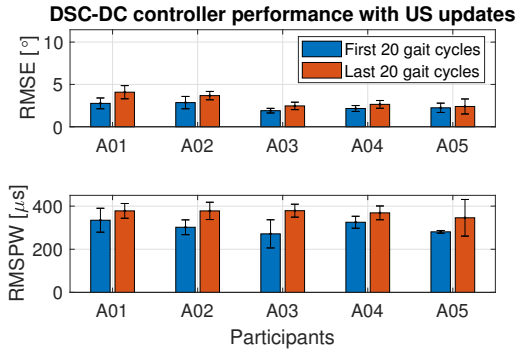


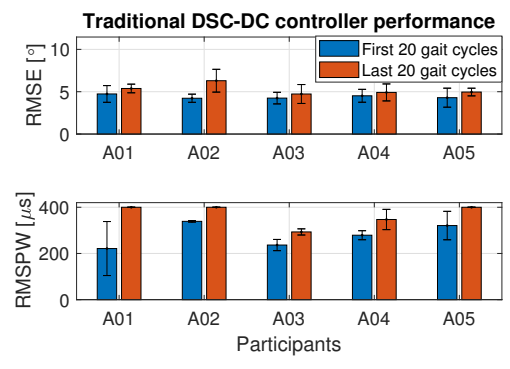
Figure 8: Experimental results of the trajectory tracking performance from 10 gait cycles by using both the US-based DSC-DC and traditional DSC-DC controllers on Participant A03. Results show the desired (dashed red curves) and actual (solid blue curves) trajectories during the swing phases.

paired t-test was performed to determine if the differences in the criteria were statistically significant at a 95% confidence level. The statistical analysis determined that the US-based DSC-DC controller statistically outperformed the traditional DSC-DC controller in the RMSE values (p < 0.001).

To further evaluate the controller performance throughout the 2-minute walking experiments in both *Task* 3 and *Task* 4, results of swing phases in the first and last 20 gait cycles within each 2-minute trial were compared and analyzed, denoted as single-task evaluation. As shown in Fig. 9 (a) and (b), the mean and SD values of the ankle joint trajectory tracking RMSE and the mean and SD values of the root mean square pulse width (RMSPW) across the first and last 20 swing phases in *Task* 3 and *Task* 4 on each participant are depicted, respectively. When either the US-based DSC-DC or the traditional DSC-DC control framework was used,



(a) The US-based DSC-DC controller in Task 3.



(b) The traditional DSC-DC controller in Task 4.

Figure 9: The mean and SD values of the dorsiflexion trajectory tracking RMSE and the FES RMSPW on the TA muscle when the US-based DSC-DC and traditional DSC-DC control frameworks were applied for each participant. (a) & (b) Results from the first 20 and last 20 swing phases in *Task* 3 and *Task* 4, respectively.

the trajectory tracking RMSE's mean value across the first 20 swing phases was lower than that across the last 20 swing phases for each participant, indicating the average ankle joint trajectory tracking performance in the first 20 gait cycles was better than the average of the last 20 gait cycles. Meanwhile, the RMSPW's mean value across the last 20 swing phases was higher than that across the first 20 swing phases for each participant, which implies that at the end of the 2-minute walking period, the FES-elicited muscle fatigue resulted in higher stimulation intensity but deteriorated the joint trajectory tracking performance.

To demonstrate the advantages of the proposed US-based DSC-DC control framework over the traditional DSC-DC control framework, results of the ankle joint trajectory tracking RMSE and TA muscle stimulation RMSPW on the same participant with different controllers were compared. Given that the FES-evoked muscle fatigue is not the focus of the current study, only results from the first 20 gait cycles in Fig. 9 were compared. Fig. 10 shows the mean trajectory tracking RMSE and mean FES RMSPW across those 20 swing cycles in *Task* 3 and *Task* 4 for each participant. A paired *t*-test was used to determine if the differences between *Task* 3 and *Task* 4 were statistically significant at a 95% confidence level across the five participants. The results in Fig. 10 (a) show

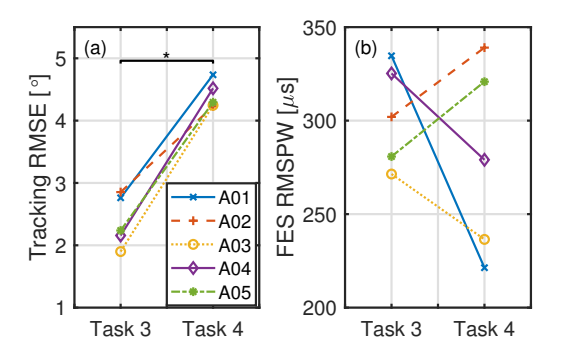
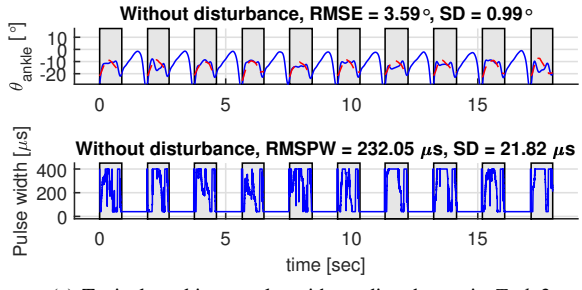


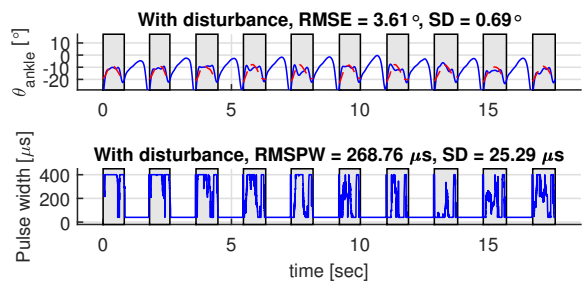
Figure 10: Comparison results of the ankle dorsiflexion trajectory tracking RMSE and FES RMSPW between Task 3 and Task 4. Each data point represents the mean value of the tracking RMSE or FES RMSPW across the first 20 swing cycles in each task on each individual participant. Asterisk  $\star$  represents the significant difference level at p < 0.001.

that the trajectory tracking RMSE values were significantly reduced by  $46.52\% \pm 7.99\%$  (p < 0.001) when the US-based DSC-DC controller was applied, compared to those when the traditional DSC-DC controller was applied. Similarly, comparison results of the TA muscle stimulation RMSPW are also presented in Fig. 10 (b). However, no statistically significant difference was observed for the RMSPW values between Task 3 and Task 4 across the five participants. The US-based DSC-DC controller thus improves tracking performance without the need for increased FES intensity.

Lastly, the robustness of the proposed US-based DSC-DC controller was evaluated by comparing the control performance in Task 3 and Task 5. To avoid the effect of FESelicited muscle fatigue, we only focused on data from the first 20 gait cycles of both tasks. Fig. 11 shows the results of plantarflexion stimulation disturbance rejection using the proposed US-based DSC-DC controller in the first 10 swing phases out of 20. During the treadmill walking in Task 5, with the motivation of the co-contraction characteristic in the drop foot syndrome, we simulated the ankle joint plantarflexion disturbance by applying a step FES input (frequency of 33 Hz, current amplitude of 25 mA, and pulse width of 100  $\mu$ s) of 500 ms on the medial and lateral gastrocnemius muscles every time when the gait cycle entered the swing phase. It is observed that an effective disturbance rejection is obtained through the proposed controller in Fig. 11 (b), where the trajectory tracking RMSE values  $(3.61\pm0.69^{\circ})$ are comparable to the situation without any disturbance  $(3.59\pm0.99^{\circ})$  in Fig. 11 (a). However, the RMSPW values  $(268.76\pm25.29 \mu s)$  when applying the disturbance are significantly higher than the situation (232.05 $\pm$ 21.82  $\mu$ s) without any disturbance (p < 0.001). Similarly, the mean and SD values of RMSE and RMSPW across the first 20 gait cycles with and without the plantarflexion disturbance on each participant are summarized in Table III. Overall, the proposed US-based DSC-DC controller still achieved a comparative ankle joint trajectory tracking performance even though a plantarflexion disturbance was added, which implied an effective disturbance rejection of the proposed control



(a) Typical tracking results without disturbance in Task 3.



(b) Typical tracking results with disturbance in Task 5.

Figure 11: The effect of disturbance rejection using the proposed US-based DSC-DC controller on Participant A03. Data come from the first 10 swing phases, and a constant plantarflexion stimulation on gastrocnemius muscles was applied throughout each swing phase as a disturbance. These plots show the desired (dashed red curves) and actual (solid blue curves) trajectories during the swing phases.

framework across these five participants.

## C. Discussion

The purpose of using US imaging in the current study was to measure the TA muscle activation level during FES, and this measurement was used as a feedback signal for the closed-loop control of the FES-elicited ankle joint neuromuscular system. US imaging directly visualizes the muscle contraction during FES and thus can monitor the muscle activation levels. It would thus act as a robust alternative to sEMG, which is often poorly suited due to interference from stimulation artifacts and cross-talk from adjacent muscles. However, US imaging for FES control is yet to be clinically translated and its advantages over sEMG must be validated in the future. That said, the real focus of the paper was not really to show an improvement of US over sEMG but to show given the potential advantages of US, how can one integrate US in closed-loop FES system control. It is true that the current US systems are more expensive and bulky than an sEMG system, and the portability of the US transducer will be critical for clinical translation of US-based drop foot technology. During the walking experiments on the treadmill, the experimental results showed that the US transducer was stabilized onto the targeted muscle steadily throughout the walking tasks (as can be seen in the newly added video demonstrations). In recently years, efforts are being made to make US imaging devices wearable [45], [61], [62], which may allow their viable integration in FES systems. Nevertheless, the comparison between the use of US imaging and sEMG signals in the closed-loop FES control problem is fairly important to further evaluate the contributions of using our proposed control framework, which will be an interesting research direction in future work. Indeed, EMG offers muscle activation at a higher frequency and our recent research [39], [41], [59] has even shown a benefit of combining US imaging, which provides mechanical information (muscle contractility) with sEMG during ankle dorsiflexion, where its electrical information can be complementary to US signals. Similar opportunity exists to combine sEMG and US for FES control and will be pursued in our future work.

The treadmill walking speed in the current study was selected as 0.6 m/s, and we have not done any testing for walking with faster speeds due to the targeted clinical population being those with drop foot syndrome who usually have slower walking speeds. We would like to infer the following implications based on the current experimental study. Firstly, the faster speeds will change the normal gait patterns, including the shank and thigh orientations and angular velocities, as well as the ankle joint trajectory during the swing phases, so the parameters need to be re-determined by using GAPSO in the virtual constraints. Secondly, given that the current US echogenicity measurement is sampled at 7.8 Hz, the faster walking speeds will shorten the time duration of the swing phase, thus reducing the available US echogenicity samples during the swing phase. These issues need to be addressed in the future US-based FES control design for faster walking speeds.

Although the two-dimensional US imaging applied in this study could visualize the skeletal muscle's architectural features from the superficial to the deep layers, it only provides information from a single plane, which might be prone to visualization errors for the targeted region of interest due to the lack of muscle depth information in the third dimension [63]. In particular, dynamic muscle contraction, including concentric and eccentric contraction, could easily cause squeeze, stretch, or overlap of muscle fascicles, and the capture of these deformations are very challenging by using two-dimensional US imaging. To address this challenge, three-dimensional US imaging has been investigated in recent years [64]. However, to our best knowledge, few studies have assessed the efficacy of real-time two-dimensional US imaging in the closed-loop control of FES systems, not to mention the real-time three-dimensional US imaging. Actually, this sort of problem is very common even for recently developed high-density sEMG (HD-sEMG) technology, where a plane of electrical information (a plane of length and width) at each time instant is provided, but HD-sEMG cannot be used to measure deeply located muscles.

There are still some limitations in the current study. The first one is that only participants without any neurological disorders were included in this study. Although they were asked to simulate the drop foot syndrome during the treadmill walking, they cannot completely avoid the volitional dorsiflexion motion during the swing phase and fully relax their foot, which was noticeable from the blue curves in

Table III: Summarized results of disturbance rejection performance by using the US-based DSC-DC controller. (Data are from the first 20 swing cycles in Task 3 and Task 5, and  $Dis_{on}$  ( $Dis_{off}$ ) represents with (without) plantarflexion disturbance.)

	A01 RMSE		A02 RMSE		A03 RMSE		A04 RMSE		A05 RMSE	
Unit [°]	Mean	SD								
$Dis_{on}$	3.61	1.38	3.15	1.66	4.07	0.74	3.38	1.26	4.18	1.89
$Dis_{off}$	2.92	1.15	2.63	0.74	3.61	0.86	3.21	0.92	3.32	1.43
	A01 RMSPW		A02 RMSPW		A03 RMSPW		A04 RMSPW		A05 RMSPW	
Unit [µs]	Mean	SD								
$Dis_{on}$	288.62	26.66	374.05	29.97	240.23	42.76	270.14	50.72	258.68	43.99
$Dis_{off}$	238.09	22.53	281.22	60.33	225.43	26.49	144.55	56.21	219.17	75.75

Fig. 6. Therefore, further evaluations of the proposed control framework on individuals with drop foot impairments are necessary in the next step. The second limitation of the applying US imaging was the low sample rate of 7.8 Hz, which was determined by the US machine in this study. Different sampling frequency rates for US data and sEMG data are due to different data acquisition mechanisms. The US data contains high dimensional signals (128 channels for the US transducer used in this study), compared to a one dimensional EMG signal (one channel per sensor). Instead, we need to transfer the raw radio frequency data (usually binarytype data) to 2D images, known as beamforming approach [60]. This beamforming procedure needs a large amount of computation and is time-consuming, which is the main reason that the US echogenicity signals can only be provided at a low-frequency rate. Transmission delays due to the use of the User Datagram Protocol (UDP) between two computer systems, e..g, the US machine with graphics processing unit (GPU) for online beamforming and US echogenicity calculation and the host computer running Simulink for the closedloop control, is another reason for low computation rates for US imaging. As for the US echogenicity computation on the US machine with GPU as mentioned in (28) and the muscle activation measurement calculation in (29), they are almost instantaneous with computation time less than 1 ms. Nevertheless, multiple options could be used to possibly increase the US sample rate. Firstly, we used 128 channels to image the TA muscle and got US echogenicity from beamformed data that were collected from all 128 channels. The reduction of the channel number would be helpful to increase the US sample rate, but could result in lower SNR. Secondly, we set the depth of US imaging as 40 mm to capture the entire region of the TA muscle. The reduction of the depth could be another option, but could result in cropped region of the TA muscle. Thirdly, applying more advanced and time-efficient beamforming algorithms or more powerful graphics processing unit could also be helpful.

# VI. CONCLUSION

In this paper, we proposed to use a US imaging-derived signal (echogenicity) as an indicator of the FES-induced muscle activation and designed an FES controller that includes both the continuous kinematic and the lower-sampled US imaging-derived activation measurements. An SDO was proposed to continuously estimate the US imaging-derived muscle activation levels during the stimulation, while a DC term was used to deal with the input delay in the muscle activation dynamics. The Lyapunov-Krasovskii stability

analysis was performed to prove the convergence of the trajectory tracking error was SGUUB. This is the first study that integrates the real-time US imaging in the closed-loop FES control. The proposed US-based DSC-DC controller was experimentally validated during the walking swing phase on a treadmill. Experimental results showed that the dorsiflexion trajectory tracking performance was significantly improved by incorporating the US-imaging signals. Future work will focus on investigation and evaluation of the proposed controller on persons with drop foot disorders, as well as the comparison between the use of US imaging and sEMG signals in the closed-loop FES control problem.

#### REFERENCES

- [1] A. K. Thompson, K. L. Estabrooks, S. Chong, and R. B. Stein, "Spinal reflexes in ankle flexor and extensor muscles after chronic central nervous system lesions and functional electrical stimulation," *Neurorehabil. Neural Repair*, vol. 23, p. 133142Wolpaw, 2009.
- [2] R. B. Stein, D. G. Everaert, A. K. Thompson, S. L. Chong, M. Whittaker, J. Robertson, and G. Kuether, "Long-term therapeutic and orthotic effects of a foot drop stimulator on walking performance in progressive and nonprogressive neurological disorders," *Neurorehabil. Neural Repair*, vol. 24, no. 2, pp. 152–167, 2010.
- [3] C. Barrett, G. Mann, P. Taylor, and P. Strike, "A randomized trial to investigate the effects of functional electrical stimulation and therapeutic exercise on walking performance for people with multiple sclerosis," *Mult. Scler. J.*, vol. 15, no. 4, pp. 493–504, 2009.
- [4] R. B. Stein, M. Bélanger, G. Wheeler, M. Wieler, D. B. Popović, A. Prochazka, and L. A. Davis, "Electrical systems for improving locomotion after incomplete spinal cord injury: An assessment," Arch. Phys. Med. Rehabil., vol. 74, no. 9, pp. 954–959, 1993.
- [5] T. Killeen, C. S. Easthope, L. Demkó, L. Filli, L. Lőrincz, M. Linnebank, A. Curt, B. Zörner, and M. Bolliger, "Minimum toe clearance: probing the neural control of locomotion," *Sci. Rep.*, vol. 7, no. 1, pp. 1–10, 2017.
- [6] A. Kantrowitz, "Electronic physiologic aids," Report of the Maimonides Hospital, pp. 4–5, 1960.
- [7] W. Liberson, "Functional electrotherapy: stimulation of the peroneal nerve synchronized with the swing phase of the gait of hemiplegic patients," Arch. Phys. Med., vol. 42, pp. 101–105, 1961.
- [8] A. I. Kottink, L. J. Oostendorp, J. H. Buurke, A. V. Nene, H. J. Hermens, and M. J. IJzerman, "The Orthotic Effect of Functional Electrical Stimulation on the Improvement of Walking in Stroke Patients with a Dropped Foot: A Systematic Review," Artif. Organs, vol. 28, no. 6, pp. 577–586, 2004.
- [9] D. G. Everaert, A. K. Thompson, S. L. Su Ling Chong, and R. B. Stein, "Does Functional Electrical Stimulation for Foot Drop Strengthen Corticospinal Connections?," *Neurorehabil. Neural Repair*, vol. 24, no. 2, pp. 168–177, 2010.
- [10] P. M. Kluding, K. Dunning, M. W. O'Dell, S. S. Wu, J. Ginosian, J. Feld, and K. McBride, "Foot Drop Stimulation Versus Ankle Foot Orthosis After Stroke," *Stroke*, vol. 44, no. 6, pp. 1660–1669, 2013.
- [11] T. Seel, C. Werner, J. Raisch, and T. Schauer, "Iterative learning control of a drop foot neuroprosthesis-generating physiological foot motion in paretic gait by automatic feedback control," *Control Eng. Pract.*, vol. 48, pp. 87–97, 2016.
- [12] T. Seel, C. Werner, and T. Schauer, "The adaptive drop foot stimulator—Multivariable learning control of foot pitch and roll motion in paretic gait," Med. Eng. Phys., vol. 38, no. 11, pp. 1205–1213, 2016.

- [13] N. Sharma, K. Stegath, C. M. Gregory, and W. E. Dixon, "Nonlinear Neuromuscular Electrical Stimulation Tracking Control of a Human Limb," *IEEE Trans. Neural Syst. Rehabil. Eng.*, vol. 17, no. 6, pp. 576– 584, 2009.
- [14] N. Sharma, C. Gregory, and W. E. Dixon, "Predictor-Based Compensation for Electromechanical Delay During Neuromuscular Electrical Stimulation," *IEEE Trans. Neural Syst. Rehabil. Eng.*, vol. 19, no. 6, pp. 601–611, 2011.
- [15] N. Alibeji, N. Kirsch, B. E. Dicianno, and N. Sharma, "A modified dynamic surface controller for delayed neuromuscular electrical stimulation," *IEEE/ASME Trans. Mechatron.*, vol. 22, pp. 1755–1764, Aug 2017.
- [16] B. C. Allen, C. A. Cousin, C. A. Rouse, and W. E. Dixon, "Robust cadence tracking for switched FES-cycling with an unknown timevarying input delay," *IEEE Trans. Control Syst. Technol.*, 2021.
- [17] N. Sharma, C. Gregory, M. Johnson, and W. Dixon, "Closed-loop neural network-based NMES control for human limb tracking," *IEEE Trans. Control Syst. Technol.*, vol. 20, no. 3, pp. 712–725, 2012.
- [18] C. A. Cousin, P. Deptula, C. A. Rouse, and W. E. Dixon, "A switched Lyapunov-passivity approach to motorized FES cycling using adaptive admittance control," *IEEE Trans. Control Syst. Technol.*, 2021.
- [19] S. Mohammed, P. Poignet, P. Fraisse, and D. Guiraud, "Toward lower limbs movement restoration with input—output feedback linearization and model predictive control through functional electrical stimulation," *Control Eng. Pract.*, vol. 20, no. 2, pp. 182–195, 2012.
- [20] N. Kirsch, N. Alibeji, and N. Sharma, "Nonlinear model predictive control of functional electrical stimulation," *Control Eng. Practice*, vol. 58, pp. 319–331, 2017.
- [21] P. Müller, A. J. Del Ama, J. C. Moreno, and T. Schauer, "Adaptive multichannel FES neuroprosthesis with learning control and automatic gait assessment," J. Neuroeng. Rehabil., vol. 17, no. 1, pp. 1–20, 2020.
- [22] Y. Li, X. Yang, Y. Zhou, J. Chen, M. Du, and Y. Yang, "Adaptive stimulation profiles modulation for foot drop correction using functional electrical stimulation: a proof of concept study," *IEEE J. Biomed. Health Inform.*, vol. 25, no. 1, pp. 59–68, 2020.
- [23] A. Page and C. Freeman, "Point-to-point repetitive control of functional electrical stimulation for drop-foot," *Control Eng. Pract.*, vol. 96, p. 104280, 2020.
- [24] A. P. L. Bo, L. O. da Fonseca, and A. C. C. de Sousa, "FES-induced coactivation of antagonist muscles for upper limb control and disturbance rejection," *Med. Eng. Phys.*, vol. 38, no. 11, pp. 1176–1184, 2016.
- [25] H. Kawai, M. J. Bellman, R. J. Downey, and W. E. Dixon, "Closed-loop position and cadence tracking control for FES-cycling exploiting pedal force direction with antagonistic biarticular muscles," *IEEE Trans. Control Syst. Technol.*, vol. 27, no. 2, pp. 730–742, 2017.
- [26] Z. Li, D. Guiraud, D. Andreu, M. Benoussaad, C. Fattal, and M. Hayashibe, "Real-time estimation of FES-induced joint torque with evoked EMG," J. Neuroeng. Rehabil., vol. 13, no. 1, p. 60, 2016.
- [27] N. Kirsch, X. Bao, N. Alibeji, B. Dicianno, and N. Sharma, "Model-based dynamic control allocation in a hybrid neuroprosthesis," *IEEE Trans. Neural Syst. Rehabil. Eng.*, vol. 26, no. 1, pp. 224–232, 2018.
- [28] H. Tankisi, D. Burke, L. Cui, M. de Carvalho, S. Kuwabara, S. D. Nandedkar, S. Rutkove, E. Stålberg, M. J. van Putten, and A. Fuglsang-Frederiksen, "Standards of instrumentation of EMG," Clin. Neurophysiol., vol. 131, no. 1, pp. 243–258, 2020.
- [29] F. Mandrile, D. Farina, M. Pozzo, and R. Merletti, "Stimulation artifact in surface EMG signal: effect of the stimulation waveform, detection system, and current amplitude using hybrid stimulation technique," *IEEE Trans. Neural Syst. Rehabil. Eng.*, vol. 11, no. 4, pp. 407–415, 2003.
- [30] C. T. Freeman, E. Rogers, A.-M. Hughes, J. H. Burridge, and K. L. Meadmore, "Iterative learning control in health care: Electrical stimulation and robotic-assisted upper-limb stroke rehabilitation," *IEEE Control Syst.*, vol. 32, no. 1, pp. 18–43, 2012.
- [31] Q. Zhang, M. Hayashibe, and C. Azevedo-Coste, "Evoked electromyography-based closed-loop torque control in functional electrical stimulation," *IEEE Trans. Biomed. Eng.*, vol. 60, no. 8, pp. 2299– 2307, 2013.
- [32] E. Ambrosini, S. Ferrante, T. Schauer, C. Klauer, M. Gaffuri, G. Ferrigno, and A. Pedrocchi, "A myocontrolled neuroprosthesis integrated with a passive exoskeleton to support upper limb activities," *J. Electromyogr. Kinesiol.*, vol. 24, no. 2, pp. 307–317, 2014.
- [33] R. Pilkar, M. Yarossi, A. Ramanujam, V. Rajagopalan, M. B. Bayram, M. Mitchell, S. Canton, and G. Forrest, "Application of empirical mode decomposition combined with notch filtering for interpretation of surface electromyograms during functional electrical stimulation,"

- *IEEE Trans. Neural Sys. Rehabil. Eng.*, vol. 25, no. 8, pp. 1268–1277, 2016.
- [34] Z. Li, D. Guiraud, D. Andreu, A. Gelis, C. Fattal, and M. Hayashibe, "Real-time closed-loop functional electrical stimulation control of muscle activation with evoked electromyography feedback for spinal cord injured patients," *Int. J. Neural Syst.*, vol. 28, no. 6, p. 1750063, 2018.
- [35] A. C. C. de Sousa, M. Valtin, A. P. Bó, and T. Schauer, "Automatic detection of stimulation artifacts to isolate volitional from evoked emg activity," *IFAC-PapersOnLine*, vol. 51, no. 27, pp. 282–287, 2018.
- [36] K. Kozasa, P. D. H. Hoang, H. Hirai, K. Hori, H. Niwa, R. Fujihara, K. Matsui, A. Nishikawa, and H. I. Krebs, "Electrical stimulation to modulate human ankle impedance: Effects of intervention on balance control in quiet and perturbed stances," in 2020 8th IEEE RAS/EMBS International Conference for Biomedical Robotics and Biomechatronics (BioRob), pp. 258–263, IEEE, 2020.
- [37] P. Hodges, L. Pengel, R. Herbert, and S. Gandevia, "Measurement of muscle contraction with ultrasound imaging," *Muscle & Nerve*, vol. 27, no. 6, pp. 682–692, 2003.
- [38] J. Shi, Y. P. Zheng, Q. H. Huang, and X. Chen, "Continuous monitoring of sonomyography, electromyography and torque generated by normal upper arm muscles during isometric contraction: sonomyography assessment for arm muscles," *IEEE Trans. Biomed. Eng.*, vol. 55, no. 3, pp. 1191–1198, 2008.
- [39] Q. Zhang, K. Kim, and N. Sharma, "Prediction of Ankle Dorsiflexion Moment by Combined Ultrasound Sonography and Electromyography," *IEEE Trans. Neural Syst. Rehabil. Eng.*, vol. 28, no. 1, pp. 318– 327, 2020.
- [40] Z. Sheng, N. Sharma, and K. Kim, "Quantitative assessment of changes in muscle contractility due to fatigue during NMES: An ultrasound imaging approach," *IEEE Trans. Biomed. Eng.*, vol. 67, no. 3, pp. 832– 841, 2019.
- [41] Q. Zhang, A. Iyer, K. Kim, and N. Sharma, "Evaluation of non-invasive ankle joint effort prediction methods for use in neurorehabilitation using electromyography and ultrasound imaging," *IEEE Trans. Biomed. Eng.*, vol. 68, no. 3, pp. 1044–1055, 2021.
- [42] Q. Zhang, A. Iyer, K. Lambeth, K. Kim, and N. Sharma, "Ultrasound echogenicity as an indicator of muscle fatigue during functional electrical stimulation," *Sensors*, vol. 22, no. 1, p. 335, 2022.
- [43] B. Ihnatsenka and A. P. Boezaart, "Ultrasound: Basic understanding and learning the language," *Int. J. Shoulder Surg.*, vol. 4, no. 3, p. 55, 2010
- [44] E. M. Strasser, T. Draskovits, M. Praschak, M. Quittan, and A. Graf, "Association between ultrasound measurements of muscle thickness, pennation angle, echogenicity and skeletal muscle strength in the elderly," Age, vol. 35, no. 6, pp. 2377–2388, 2013.
- [45] S. Sikdar, H. Rangwala, E. B. Eastlake, I. A. Hunt, A. J. Nelson, J. Devanathan, A. Shin, and J. J. Pancrazio, "Novel method for predicting dexterous individual finger movements by imaging muscle activity using a wearable ultrasonic system," *IEEE Trans. Neural Syst. Rehabil. Eng.*, vol. 22, no. 1, pp. 69–76, 2013.
- [46] R. D. Gregg, T. Lenzi, L. J. Hargrove, and J. W. Sensinger, "Virtual constraint control of a powered prosthetic leg: From simulation to experiments with transfermoral amputees," *IEEE Trans. Robot.*, vol. 30, no. 6, pp. 1455–1471, 2014.
- [47] Q. Zhang, A. Iyer, Z. Sun, A. Dodson, and N. Sharma, "Sampled-data observer based dynamic surface control of delayed neuromuscular functional electrical stimulation," in *Dynamic Systems and Control Conference*, vol. 84270, p. V001T14A003, American Society of Mechanical Engineers, 2020.
- [48] R. Riener and T. Fuhr, "Patient-driven control of FES-supported standing up: A simulation study," *IEEE Trans. Rehabil. Eng.*, vol. 6, pp. 113–124, 1998.
- [49] H. Hatze, "A myocybernetic control model of skeletal muscle," *Biol. Cybern.*, vol. 25, no. 2, pp. 103–119, 1977.
- [50] D. A. Winter, Biomechanics and motor control of human movement. John Wiley & Sons, 2009.
- [51] T. Schauer, N. O. Negard, F. Previdi, K. J. Hunt, M. H. Fraser, E. Ferchland, and J. Raisch, "Online identification and nonlinear control of the electrically stimulated quadriceps muscle," *Control Eng. Pract.*, vol. 13, pp. 1207–1219, 2005.
- [52] D. Zhang and Y. Shen, "Continuous sampled-data observer design for nonlinear systems with time delay larger or smaller than the sampling period," *IEEE Trans. Automat. Contr.*, vol. 62, no. 11, pp. 5822–5829, 2016

- [53] T. Ahmed-Ali, V. Van Assche, J.-F. Massieu, and P. Dorleans, "Continuous-Discrete Observer for State Affine Systems With Sampled and Delayed Measurements," *IEEE Trans Automat Contr*, vol. 58, no. 4, pp. 1085–1091, 2013.
- [54] D. Zhang and Y. Shen, "Global output feedback sampled-data stabilization for upper-triangular nonlinear systems with improved maximum allowable transmission delay," *Int. J. Robust Nonlinear Control*, vol. 27, no. 2, pp. 212–235, 2017.
- [55] E. R. Westervelt, J. W. Grizzle, and D. E. Koditschek, "Hybrid zero dynamics of planar biped walkers," *IEEE Trans. Automat. Contr.*, vol. 48, no. 1, pp. 42–56, 2003.
- [56] V. Molazadeh, Q. Zhang, X. Bao, and N. Sharma, "An Iteratively Learning Time-Invariant Controller for a Switched Cooperative Allocation Strategy during Sit-to-Stand Task with a Hybrid Exoskeleton," *IEEE Trans. Control Syst. Technol.*, vol. 30, no. 3, pp. 1021–1036, 2022.
- [57] Y. Marinakis and M. Marinaki, "A hybrid genetic-particle swarm optimization algorithm for the vehicle routing problem," *Expert Syst. Appl.*, vol. 37, no. 2, pp. 1446–1455, 2010.
- [58] Y. Liu, Z. Wang, and X. Liu, "On global exponential stability of generalized stochastic neural networks with mixed time-delays," *Neu*rocomputing, vol. 70, no. 1-3, pp. 314–326, 2006.
- [59] Q. Zhang, A. Iyer, Z. Sun, K. Kim, and N. Sharma, "A Dual-modal Approach Using Electromyography and Sonomyography Improves Prediction of Dynamic Ankle Dorsiflexion Motion," *IEEE Trans. Neural Syst. Rehabil. Eng.*, vol. 29, pp. 1944–1954, 2021.
- [60] K. E. Thomenius, "Evolution of ultrasound beamformers," in 1996 IEEE Ultrasonics Symposium. Proceedings, vol. 2, pp. 1615–1622, IEEE, 1996.
- [61] N. Akhlaghi, C. A. Baker, M. Lahlou, H. Zafar, K. G. Murthy, H. S. Rangwala, J. Kosecka, W. M. Joiner, J. J. Pancrazio, and S. Sikdar, "Real-Time Classification of Hand Motions Using Ultrasound Imaging of Forearm Muscles," *IEEE Trans Biomed Eng*, vol. 63, no. 8, pp. 1687–1698, 2016.
- [62] X. Yang, Z. Chen, N. Hettiarachchi, J. Yan, and H. Liu, "A wearable ultrasound system for sensing muscular morphological deformations," *IEEE Trans. Syst. Man Cybern.: Syst.*, vol. 51, no. 6, pp. 3370–3379, 2019.
- [63] T. J. Roberts, C. M. Eng, D. A. Sleboda, N. C. Holt, E. L. Brainerd, K. K. Stover, R. L. Marsh, and E. Azizi, "The multi-scale, threedimensional nature of skeletal muscle contraction," *Physiology*, vol. 34, no. 6, pp. 402–408, 2019.
- [64] B. J. Raiteri, A. G. Cresswell, and G. A. Lichtwark, "Three-dimensional geometrical changes of the human tibialis anterior muscle and its central aponeurosis measured with three-dimensional ultrasound during isometric contractions," *PeerJ*, vol. 4, p. e2260, 2016.

## Appendix

A Lyapunov-Krasovskii method-based stability analysis is used to determine the sufficient conditions and guarantee the closed-loop error system in (23) is SGUUB. To facilitate the following analysis, three continuously differentiable, nonnegative, radially unbounded functions are defined as

$$V_1(t) = \frac{1}{2}e_0^2 + \frac{1}{2}e_1^2 + \frac{1}{2}J_{\Gamma}e_2^2 + \frac{1}{2}\varepsilon_3^2 + \frac{1}{2}S_n^2 + \frac{1}{2}y_f^2 , \quad (30)$$

$$P(t) = \frac{\zeta_3}{\beta^2} \int_{t-\tau_M}^t \left( \int_s^t u^2(\omega) d\omega \right) ds, \ t \in [t_0, \infty),$$
 (31)

$$Q(t) = \gamma \int_{t-\bar{T}}^{t} \left( \int_{\rho}^{t} \varepsilon_{3}^{2}(s) ds \right) d\rho, \ t \in [t_{0}, \infty),$$
 (32)

where  $V_1(t)$  can be bounded as  $\underline{m} \|w\|^2 \leq V_1(t) \leq \overline{m} \|w\|^2$ ,  $w \in \mathbb{R}^6$   $w = [e_0, \, e_1, \, e_2, \, \varepsilon_3, \, S_n, \, y_f]^T$ , and  $\underline{m}, \, \overline{m} \in \mathbb{R}^+$  are known positive constants defined as  $\underline{m} \triangleq \frac{1}{2} \min{(1, \, a_1)}$  and  $\overline{m} \triangleq \frac{1}{2} \max{(1, \, a_2)}$ . The vector  $\chi \in \mathcal{L} \subset \mathbb{R}^8$  is defined as

$$\chi = \left[ w^T, \sqrt{P}, \sqrt{Q} \right]^T. \tag{33}$$

*Proof:* A Lyapunov-Krasovskii (LK) functional candidate  $V(\chi,t):\mathcal{L}\times[t_0,\infty)\to\mathbb{R}^+$  is defined as

$$V(\chi, t) = V_1(t) + P(t) + Q(t), \tag{34}$$

and  $V(\chi, t)$  can be lower and upper bounded as

$$\underline{\lambda} \|\chi\|^2 \le V(\chi, t) \le \overline{\lambda} \|\chi\|^2, \tag{35}$$

where  $\lambda, \overline{\lambda} \in \mathbb{R}^+$  are constant values.

By taking the time derivative of (34), we can get

$$\dot{V} = e_0 \dot{e}_0 + e_1 \dot{e}_1 + J_{\Gamma} e_2 \dot{e}_2 + \frac{1}{2} \dot{J}_{\Gamma} e_2^2 + \varepsilon_3 \dot{\varepsilon}_3 
+ S_n \dot{S}_n + y_f \dot{y}_f + \dot{P} + \dot{Q},$$
(36)

where  $\dot{y}_f = \dot{x}_{3d} - \dot{x}_{3f} = \dot{x}_{3d} - \frac{y_f}{\zeta_3}$ . To get the explicit expressions of  $\dot{P}$  and  $\dot{Q}$ , the Leibniz integral rule needs to be applied. By denoting  $\eta = \dot{x}_{3d}$  as a continuous nonlinear function and using (7), (12), (13), (14), (20), (23), (25), and (26), the time-derivative of V can be upper bounded as

$$\dot{V} \leq -\alpha_{0}e_{0}^{2} - \alpha_{1}e_{1}^{2} - Ke_{2}^{2} - \left(\frac{1}{T_{a}} - \gamma \bar{T}\right)\varepsilon_{3}^{2} \\
- \left(\beta - \frac{\zeta_{3}\tau_{M}}{\delta^{2}}\right)S_{n}^{2} + |e_{2}||S_{n}| + |e_{2}||y_{f}| + |e_{2}||\varepsilon_{3}| \\
+ |e_{2}|\rho\left(||z||\right)||z|| + |e_{2}|\zeta + |e_{0}||e_{1}| + |y_{f}||\eta| \\
+ |S_{n}|\left|\left(\frac{\hat{x}_{3}}{T_{a}} + \left(\delta - \frac{1}{T_{a}}\right)u(t - \tau_{M})\right)\right| + \gamma\bar{\varepsilon}_{3}^{k}|\varepsilon_{3}| \\
- \left(\frac{1}{\zeta_{3}} - \frac{\tau_{M}}{\delta^{2}\beta^{2}\zeta_{3}}\right)y_{f}^{2} + \frac{2\tau_{M}}{\delta^{2}\beta}|S_{n}||y_{f}| + \gamma\bar{\varepsilon}_{3}^{k}|S_{n}| \\
- \frac{\zeta_{3}}{\beta^{2}}\int_{t - \tau_{M}}^{t} u^{2}(s)ds - \gamma\int_{t - \bar{T}}^{t}\varepsilon_{3}^{2}(s)ds. \tag{37}$$

Based on Young's inequality and Assumption 1, 2, and 4, the following terms will be bounded as

$$\begin{aligned} |e_{0}| |e_{1}| &\leq \frac{1}{2} \left( e_{0}^{2} + e_{1}^{2} \right), |e_{2}| |S_{n}| \leq \frac{1}{2} \left( e_{2}^{2} + S_{n}^{2} \right), \\ |e_{2}| |\varepsilon_{3}| &\leq \frac{1}{2} \left( e_{2}^{2} + \varepsilon_{3}^{2} \right), |e_{2}| |y_{f}| \leq \frac{1}{2} \left( e_{2}^{2} + y_{f}^{2} \right), \\ |y_{f}| |\eta| &\leq \frac{1}{2} \left( \frac{1}{\epsilon} y_{f}^{2} \eta^{2} + \epsilon \right), |S_{n}| |y_{f}| \leq \frac{1}{2} \left( S_{n}^{2} + y_{f}^{2} \right), \\ |S_{n}| \left| \frac{\hat{x}_{3}}{T_{a}} + \left( \delta - \frac{1}{T_{a}} \right) u(t - \tau_{M}) \right| \leq \psi |S_{n}| \leq \frac{\psi^{2} S_{n}^{2}}{2\epsilon} + \frac{\epsilon}{2}, \\ \bar{\varepsilon}_{3}^{k} |\varepsilon_{3}| &\leq \frac{1}{2} \left( \frac{1}{\epsilon} (\bar{\varepsilon}_{3}^{k})^{2} \varepsilon_{3}^{2} + \epsilon \right), \bar{\varepsilon}_{3}^{k} |S_{n}| \leq \frac{1}{2} \left( \frac{1}{\epsilon} (\bar{\varepsilon}_{3}^{k})^{2} S_{n}^{2} + \epsilon \right), \end{aligned}$$

where  $\epsilon \in \mathbb{R}^+$  is an arbitrary constant, and  $\psi \in \mathbb{R}^+$  is the upper bound of  $\left|\frac{\hat{x}_3}{T_a} + \left(\delta - \frac{1}{T_a}\right)u(t - \tau_M)\right|$ . By applying the inequalities in (38) to (37), the inequality can be further simplified as

$$\dot{V} \leq -\left(\alpha_{0} - \frac{1}{2}\right)e_{0}^{2} - \left(\alpha_{1} - \frac{1}{2}\right)e_{1}^{2} - \left(K - \frac{3}{2}\right)e_{2}^{2} \\
-\left(\frac{1}{T_{a}} - \gamma\bar{T} - \frac{1}{2} - \frac{\gamma(\bar{\varepsilon}_{3}^{k})^{2}}{2\epsilon}\right)\varepsilon_{3}^{2} + |e_{2}|\zeta \\
+ |e_{2}|\rho\left(\|z\|\right)\|z\| - \left(\beta - \frac{\tau_{M}}{\delta^{2}\beta} + \vartheta\right)S_{n}^{2} \\
+ (1 + \gamma)\epsilon - \frac{\zeta_{3}}{\beta^{2}}\int_{t - \tau_{M}}^{t} u^{2}(s)ds \\
-\left(\frac{\kappa}{\zeta_{3}} - \frac{1}{2} - \frac{\eta^{2}}{2\epsilon} - \frac{\tau_{M}}{\delta^{2}\beta}\right)y_{f}^{2} - \gamma\int_{t - \bar{T}}^{t}\varepsilon_{3}^{2}(s)ds, \quad (39)$$

where  $\vartheta=-rac{\zeta_3 au_M}{\delta^2}-rac{1}{2}-rac{\psi^2}{2\epsilon}-rac{\gamma(ar{arepsilon}_3^k)^2}{2\epsilon}$  and  $\kappa=1-rac{ au_M}{\delta^2eta^2}$ . The coefficient  $rac{\kappa}{\zeta_3}-rac{1}{2}-rac{\eta^2}{2\epsilon}-rac{ au_M}{\delta^2eta}$  needs to be a positive constant by defining the control gain  $\zeta_3$  as

$$\frac{1}{\zeta_3} > \frac{1}{\kappa} \left[ \frac{1}{2} + \frac{\bar{\eta}^2}{2\epsilon} + \frac{\tau_M}{\delta^2 \beta} \right],\tag{40}$$

where  $\bar{\eta} \in \mathbb{R}^+$  is the maximum of  $\eta$  in the defined compact set  $\Xi = \left\{ \chi \in \mathbb{R}^8 | \ \|\chi\| < \sigma, \ \chi = \left[ w, \sqrt{P}, \sqrt{Q} \right]^T \right\}$  and  $\sigma \in$ 

 $\mathbb{R}^+$  is a known constant in the compact set. Recall the control gain  $K=K_1+K_2+K_3$ . After completing the squares to compensate for  $|e_2|\zeta$  and  $\rho\left(\|z\|\right)\|z\|$  using  $(K_2+K_3)\,e_2^2$ , the following inequality can be obtained

$$\begin{split} \dot{V} &\leq -\left(\alpha_{0} - \frac{1}{2}\right)e_{0}^{2} - \left(\alpha_{1} - \frac{1}{2}\right)e_{1}^{2} - \left(K_{1} - \frac{3}{2}\right)e_{2}^{2} \\ &- \left(\frac{1}{T_{a}} - \gamma \bar{T} - \frac{1}{2} - \frac{\gamma(\bar{\varepsilon}_{3}^{k})^{2}}{2\epsilon}\right)\varepsilon_{3}^{2} + \frac{\zeta^{2}}{4K_{3}} \\ &+ (1 + \gamma)\epsilon + \frac{\left(\rho\left(\left\|z\right\|\right)\left\|z\right\|\right)^{2}}{4K_{2}} - \left(\beta - \frac{\tau_{M}}{\delta^{2}\beta} + \vartheta\right)S_{n}^{2} \\ &- \left(\frac{\kappa}{\zeta_{3}} - \frac{1}{2} - \frac{\eta^{2}}{2\epsilon} - \frac{\tau_{M}}{\delta^{2}\beta}\right)y_{f}^{2} \\ &- \frac{\zeta_{3}}{\beta^{2}}\int_{t-\tau_{M}}^{t} u^{2}(s)ds - \gamma \int_{t-\bar{T}}^{t} \varepsilon_{3}^{2}(s)ds. \end{split} \tag{41}$$

Recall  $e_I(t) = \int_{t-\tau_M}^t u(s)ds$ , by using Lemma 1, we have

$$e_I^2(t) = \left(\int_{t-\tau_M}^t u(s)ds\right)^2 \le \tau_M \int_{t-\tau_M}^t u(s)^2 ds.$$
 (42)

Then by multiplying  $-\frac{\zeta_3}{2\tau_M\beta^2}$ , the inequality is given as

$$-\frac{\zeta_3}{2\tau_M\beta^2} \left(\tau_M \int_{t-\tau_M}^t u(s)^2 ds\right) \le -\frac{\zeta_3}{2\tau_M\beta^2} e_I^2. \tag{43}$$

Therefore, (41) can be simplified as

$$\dot{V} \leq -\left(\xi - \frac{\rho^2\left(\|z\|\right)}{4K_2}\right)\|z\|^2 - \left(\beta - \frac{\tau_M}{\delta^2\beta} + \vartheta\right)S_n^2 \\
-\left(\frac{1}{T_a} - \gamma \bar{T} - \frac{1}{2} - \frac{\gamma(\bar{\varepsilon}_3^k)^2}{2\epsilon}\right)\varepsilon_3^2 + \frac{\zeta^2}{4K_3} \\
-\left(\frac{\kappa}{\zeta_3} - \frac{1}{2} - \frac{\eta^2}{2\epsilon} - \frac{\tau_M}{\delta^2\beta}\right)y_f^2 + (1+\gamma)\epsilon \\
-\frac{\zeta_3}{2\beta^2} \int_{t=T,V}^t u^2(s)ds - \gamma \int_{t=\bar{T}}^t \varepsilon_3^2(s)ds, \tag{44}$$

where  $\xi = \min \left\{ \alpha_0 - \frac{1}{2}, \, \alpha_1 - \frac{1}{2}, \, K_1 - \frac{3}{2}, \, \frac{\zeta_3}{2\tau_M\beta^2} \right\}$ . Given that the Krasovskii functional candidates P and Q could be bounded as follows

$$\begin{split} P & \leq \frac{\zeta_3 \tau_M}{\beta^2} \sup_{s \in (t - \tau_M, \, t)} \left( \int_s^t u^2(w) dw \right) = \frac{\zeta_3 \tau_M}{\beta^2} \int_{t - \tau_M}^t u^2(w) dw, \\ Q & \leq \gamma \bar{T} \sup_{\rho \in (t - \bar{T}, \, t)} \left( \int_\rho^t \varepsilon_3^2(s) ds \right) = \gamma \bar{T} \int_{t - \bar{T}}^t \varepsilon_3^2(s) ds, \end{split}$$

the equation (44) can be rewritten as

$$\dot{V} \leq -\left(\xi - \frac{\rho^2(\|z\|)}{4K_2}\right) \|z\|^2 - \left(\beta - \frac{\tau_M}{\delta^2\beta} + \vartheta\right) S_n^2 
- \left(\frac{1}{T_a} - \gamma \bar{T} - \frac{1}{2} - \frac{\gamma(\bar{\varepsilon}_3^k)^2}{2\epsilon}\right) \varepsilon_3^2 + \frac{\zeta^2}{4K_3} + (1+\gamma)\epsilon 
- \left(\frac{\kappa}{\zeta_3} - \frac{1}{2} - \frac{\eta^2}{2\epsilon} - \frac{\tau_M}{\delta^2\beta}\right) y_f^2 - \frac{1}{2\tau_M} P - \frac{1}{\bar{T}} Q.$$
(45)

According to the definition of z(t) and  $\chi(t)$ , the equation (45) can be upper bounded as

$$\dot{V} \le -\left\{\xi - \frac{\rho^2(\|z\|)}{4K_2}\right\} \|e_I\|^2 - \underline{\xi} \|\chi\|^2 + \varsigma, \tag{46}$$

where  $\varsigma = \frac{\zeta^2}{4K_3} + (1+\gamma)\epsilon$ , which is bounded by  $\bar{\varsigma} \in \mathbb{R}^+$ , and  $\xi(\|\chi\|) \in \mathbb{R}^+$  is defined as

$$\begin{split} \underline{\xi}\left(\|\chi\|\right) &= & \min\Big\{\frac{1}{T_a} - \gamma \bar{T} - \frac{1}{2} - \frac{\gamma(\bar{\varepsilon}_3^k)^2}{2\epsilon}, \, \xi - \frac{\rho^2(\|z\|)}{4K_2}, \\ \beta - \frac{\tau_M}{\delta^2\beta} + \vartheta, \, \frac{\kappa}{\zeta_2} - \frac{1}{2} - \frac{\eta^2}{2\epsilon} - \frac{\tau_M}{\delta^2\beta}, \, \frac{1}{2\tau_M}, \, \frac{1}{\bar{T}}\Big\}. \end{split}$$

The expression (46) can be further bounded when it satisfies the condition  $\xi - \frac{\rho^2(\|z\|)}{4K_2} \ge 0$ , which is true if the condition  $\|z\|^2 \le \rho^{-2} \left(2\sqrt{K_2\xi}\right)$  is satisfied, which implies  $\dot{V} \le -\xi \|\chi\|^2 + \bar{\varsigma}$ . Given the boundary conditions in (35) and the definition of z and  $\chi$ , a set for the initial condition of the augmented state vector  $\chi(t)$  can be defined as

$$\mathcal{F} \triangleq \left\{ \chi(t) \in \mathbb{R}^8 | \| \chi(0) \| = \sigma < \sqrt{\frac{\lambda}{\bar{\lambda}} \left[ \min \left\{ 1, \frac{\zeta_3}{\tau_M \beta^2} \right\} \rho^{-2} \left( 2\sqrt{K_2 \xi} \right) - \bar{\varsigma} \right]} \right\}, \tag{47}$$

where the compact set,  $\Xi = \left\{\chi \in \mathbb{R}^8 | \, \|\chi\| < \sigma, \, \chi = \left[w, \sqrt{P}, \sqrt{Q}\right]^T\right\}$  must satisfy  $\|\chi(0)\| = \sigma$  to ensure  $\bar{\eta} \in \mathbb{R}^+$  in (40) exists in the defined compact set. Based on the conditions in Theorem 1,  $\underline{\xi}\left(\|\chi\|\right) \geq 0$  always holds and it can be lower bounded by a positive constant  $\varpi \leq \underline{\xi}\left(\|\chi\|\right) \in \mathbb{R}_{\geq 0}$ . Recall the upper bound of V in (35), the inequality in (46) is rewritten as

$$\dot{V} \leq -\frac{\overline{\omega}}{\overline{\lambda}}V + \overline{\varsigma} . \tag{48}$$

Therefore, for  $\chi(0)\in\mathcal{F},$  the solution of the linear differential equation (48) is computed as

$$V(\chi(t)) \le V(0)e^{-\frac{\varpi}{\lambda}t} + \frac{\overline{\lambda}\overline{\varsigma}}{\varpi} \left(1 - e^{-\frac{\varpi}{\lambda}t}\right), t \in [t_0, \infty).$$
 (49)

Consider the lower and upper bounds of the LK functional candidate in (35). The augmented state vector  $\chi(t)$  can be upper bounded as

$$\|\chi(t)\| \le \sqrt{\frac{\overline{\lambda}}{\underline{\lambda}}} \left( \|\chi(0)\|^2 - \frac{\overline{\varsigma}}{\varpi} \right) e^{-\frac{\varpi}{2\overline{\lambda}}t} + \sqrt{\frac{\overline{\lambda}\overline{\varsigma}}{\underline{\lambda}\varpi}}.$$
 (50)

Given the definition of  $\|\chi(t)\|$  and the relationship in (12), the explicit boundary of the trajectory tracking error, defined in (27), can be expressed as

$$|e(t)| \leq (1 + \alpha_0) \left[ \sqrt{\frac{\overline{\lambda}}{\underline{\lambda}} \left( \|\chi(0)\|^2 - \frac{\overline{\varsigma}}{\varpi} \right)} e^{-\frac{\varpi}{2\overline{\lambda}}t} + \sqrt{\frac{\overline{\lambda}\overline{\varsigma}}{\underline{\lambda}\varpi}} \right].$$

From (49), by providing the control gains  $\alpha_0$ ,  $\alpha_1$ ,  $K_1$ ,  $K_2$ ,  $\beta$ , and  $\delta$ , as well as the observation gain  $\gamma$  according to the sufficient conditions in Theorem 1,  $V(\chi(t))$  decays exponentially to a boundary  $\frac{\overline{\lambda}\overline{\epsilon}}{\varpi}$ . Because  $V\in\mathcal{L}_{\infty}$ , the state variables in the augmented vector  $e_0,\,e_1,\,e_2,\,S_n,\,\varepsilon_3,\,y_f,\,\sqrt{P},\,\sqrt{Q}\in\mathcal{L}_{\infty}$ . From (50), the compact set  $\Xi=\left\{\chi\in\mathbb{R}^8|\,\|\chi(0)\|=\sigma,\,\chi=\left[w,\,\sqrt{P},\,\sqrt{Q}\right]^T\right\}$  is invariant. This implies  $\bar{\eta}\in\mathbb{R}^+$ , the maximum of  $\eta$  in the compact set  $\Xi$ , exists and thus  $\dot{x}_{3d}\in\mathcal{L}_{\infty}$ . Recalling the lower bound of V in (35), further analysis can be done to show the ultimate bound of  $\|\chi\|$  is  $\sqrt{\frac{\overline{\lambda}\overline{\epsilon}}{\lambda}\varpi}$ , while the ultimate bound of |e| is  $(1+\alpha_0)\sqrt{\frac{\overline{\lambda}\overline{\epsilon}}{\lambda}\varpi}$ . Therefore, we can conclude that the closed-loop system is SGUUB.